Physics of the Earth and Planetary Interiors 286 (2019) 111–126

Contents lists available at ScienceDirect

Physics of the Earth and Planetary Interiors

journal homepage: www.elsevier.com/locate/pepi

Causes for polarity reversals of PP precursor waves reflecting off the 410 km discontinuity beneath the Atlantic

Morvarid Saki[a,*], Christine Thomas[a], Laura Cobden[b], Rafael Abreu[a], Johannes Buchen[c]

[a] Institute of Geophysics, University of Münster, Corrensstr. 24, 48149 Münster, Germany
[b] Department of Earth Sciences, Utrecht, Vening Meineszgebouw A, Princetonlaan 8a, 3584 CB Utrecht, Netherlands
[c] Bayerisches Geoinstitut (BGI), University of Bayreuth, Universitätsstr. 30, 95447 Bayreuth, Germany

ABSTRACT

We investigate the velocity and density structure of the mantle beneath the Northern Atlantic at a depth of 410 km where the olivine to wadsleyite phase transformation occurs. Measuring polarities of precursor arrivals to PP seismic waves that reflect at this transition we analyze over 1700 teleseismic seismograms from 13 different source-receiver combinations using the advantages of high-resolution array seismology methods and crossing ray paths. The final dataset consists of 45 events with $M_w \geq 5.8$ with a good coverage of reflection points beneath the investigation area. We find several events where the polarity of the precursor signal is opposite to that of the PP wave, however, events with same polarity of precursor and PP wave are also observed. We test several causes for changing polarity of reflections at the 410 km discontinuity and find out that there is a dependence of the polarity on epicentral distance. We computed the reflection coefficients of the precursor wave using the Zoeppritz equations with the initial values of density, V_P and V_S of a pyrolite model for the olivine-wadsleyite phase transition and varied the values by ± 10% above and below 410 km depth. More than 729 million combinations of density, compressional and shear wave velocities for olivine and wadsleyite layers were tested to find the combinations that can explain our polarity-distance observations. While the best-fitting models have a smaller positive contrast than pyrolite in density, a small negative contrast for P and S wave velocities is needed. Possibilities to explain these values include combination of a hydrous wadsleyite layer beneath, and anhydrous or Fe-enriched olivine above the boundary.

1. Introduction

The 410 and 660 km seismic discontinuities which mark the top and bottom boundaries of the mantle transition zone (e.g., Bina and Helffrich, 1994; Helffrich, 2000; Frost, 2008) are established as a prominent feature in almost all 1-D reference Earth models, for instance IASP91 (Kennett and Engdahl, 1991) or AK135 (Kennett et al., 1995). While the 410 km discontinuity is described by P and S wave velocity increases of +3.7% (P wave) and +4.3% (S wave) and density jump of + 4.8% (e.g., Lawrence and Shearer, 2006), the 660 km boundary is associated with velocity jumps of +4.5% and +6.8% for P and S wave respectively, and density increase of 4.4% (e.g., Lawrence and Shearer, 2006).

The mantle transition zone discontinuities are generally explained by phase transformations of olivine to the high-pressure-polymorphs, wadsleyite (β-spinel) at depths around 410 km (e.g., Akaogi et al., 1989; Katsura and Ito, 1989; Helffrich, 2000; Katsura et al., 2004), and to ringwoodite (γ-spinel) at around 520 km. Ringwoodite transforms to a mixture of bridgmanite and magnesiowüstite at 660 km depth (e.g., Ito and Takahashi, 1989; Wood and Rubie, 1996; Shim et al., 2001; Fei et al., 2004). However, it is still debated whether this set of phase transitions is the only responsible source for the presence of discontinuities or whether additional changes in chemistry are also required to create the observed change in density and wave velocities (e.g., Gu et al., 2001).

The depth and width of the transition zone discontinuities are strongly affected by thermal variations in the mantle as predicted by the Clapeyron slopes of the phase transitions (e.g., Weidner and Wang, 2000; Andrews and Deuss, 2008; Deuss, 2009; Saki et al., 2015). Several seismic studies at regional and global scale (e.g., Flanagan and Shearer, 1999; Gurrola and Minster, 2000; Chambers et al., 2005; Deuss, 2007, 2009; Bonatto et al., 2013; Saki et al., 2015; Jenkins et al., 2016; Yu et al., 2017) support this hypothesis. Compositional variations, however, can also change the depth and thickness of the phase transformation. For instance, water has a strong influence on the sharpness of the upper mantle discontinuities: in hydrous mantle the 410 km boundary can broaden up to 40 km compared to 12 km in the anhydrous system (e.g., Wood, 1995; Helffrich and Wood, 1996; Smyth and Frost, 2002).

Additionally, the Al and Fe content of the pyrolite-system may cause more complicated phase transitions and play an important role in the topography of the mantle transition zone (e.g., Helffrich, 2000;

* Corresponding author.
E-mail addresses: msaki_01@uni-muenster.de (M. Saki), cthomas_01@earth.uni-muenster.de (C. Thomas), l.j.cobden@uu.nl (L. Cobden), abreu@uni-muenster.de (R. Abreu), Johannes.buchen@uni-bayreuth.de (J. Buchen).

https://doi.org/10.1016/j.pepi.2018.11.007
Received 6 June 2018; Received in revised form 15 November 2018; Accepted 26 November 2018
Available online 27 November 2018
0031-9201/

Weidner and Wang, 2000; Hirose, 2002; van der Meijde et al., 2003; Katsura et al., 2004; Deuss et al., 2006; Frost and Dolejs, 2007; Schmerr and Thomas, 2011). The amount of Al_2O_3 controls the degree of the pyroxene to garnet transformation (e.g., Irifune et al., 1998; Weidner and Wang, 2000). The Al content of the composition therefore affects the amount of pyroxene and garnet in the system. The olivine-system is in a reciprocal interaction with the pyroxene-garnet system by Fe partitioning. In a low Al_2O_3 bearing system, the pyroxene to garnet phase transformation could be spread out over 3 GPa (i.e., ~80–90 km) and pyroxene transforms into wadsleyite plus stishovite near 410 km depth and leads to a broader 410 km discontinuity (e.g., Weidner and Wang, 2000). In the case of higher Al content, pyroxene transforms into garnet. Since garnet tends to take Fe from olivine or wadsleyite, the Fe-poor composition makes the discontinuity narrower and shifts it to deeper depths (Weidner and Wang, 2000). The width of the pressure interval of the olivine to wadsleyite phase transition has been estimated to be ~6 km in dry pyrolite (Frost, 2003b) and may go up to 13 km, when considering Fe-Mg partitioning effects (Katsura et al., 2004).

The upper mantle seismic discontinuities have been detected in numerous studies using global SS precursor datasets (e.g., Gossler and Kind, 1996; Flanagan and Shearer, 1998; Schmerr and Garnero, 2006; Lawrence and Shearer, 2008; Houser et al., 2008; Deuss, 2009; Gu et al., 2009), PP precursor datasets (e.g., Flanagan and Shearer, 1999; Deuss, 2009; Thomas and Billen, 2009), direct measurements of P wave apparent velocities (Niazi and Anderson, 1965), short period PKPPKP ($P\dot{P}\dot{P}$) underside reflections (e.g., Benz and Vidale, 1993; Day and Deuss, 2013) and P to S conversions (e.g., Petersen et al., 1993; Vinnik, 1977; Kind et al., 2002; Andrews and Deuss, 2008).

Precursors to the phases PP and SS waves are generated by reflections of P (or S) waves on the underside of mantle discontinuities (Fig. 1). Those precursors, despite having weak amplitudes (e.g., Flanagan and Shearer, 1998, 1999; Deuss, 2007, 2009; Schmerr and Garnero, 2007; Schmerr and Thomas, 2011; Lessing et al., 2015; Saki et al., 2015), are widely used to establish the presence and properties of transition zone discontinuities such as the magnitude and sign of the velocity and density jump across the boundaries (e.g., Flanagan and Shearer, 1998; Deuss and Woodhouse, 2001; Gu and Dziewonski, 2002; Houser et al., 2008; Saki et al., 2015; Reiss et al., 2017). PP and SS precursors are sensitive to the mid-point between the source and receiver. This means that precursor waves, enable us to investigate the oceanic regions, which cannot be sampled by other methods such as receiver functions which are sensitive to the structure beneath the station.

The amplitude of reflected waves depends on the contrast of elastic parameters across the boundary as well as the sharpness of the discontinuity. However, topography can also influence the amplitude (e.g., Flanagan and Shearer, 1999; Chambers et al., 2005; Schmerr and Thomas, 2011; Rychert et al., 2013; Lessing et al., 2015). Current measurements of the reflection coefficient and impedance contrast across the 410 km discontinuity are mostly confined to regional studies (e.g., Vidale and Benz, 1992; Revenaugh and Sipkin, 1994; Rost and Weber, 2002).

The global reference models such as AK135 (Kennett et al., 1995; Engdahl et al., 1998) provide a very good first-order fit to seismic wave travel times. However, the waveforms, amplitudes, and polarities of arrivals corresponding to reflections of upper mantle discontinuities are not always consistent with AK135. The non-detections of PP wave precursors at regional scale reported by Estabrook and Kind (1996), strong amplitude variation shown by Lessing et al. (2015) as well as the observations of polarity reversals of the reflection from the 410 and

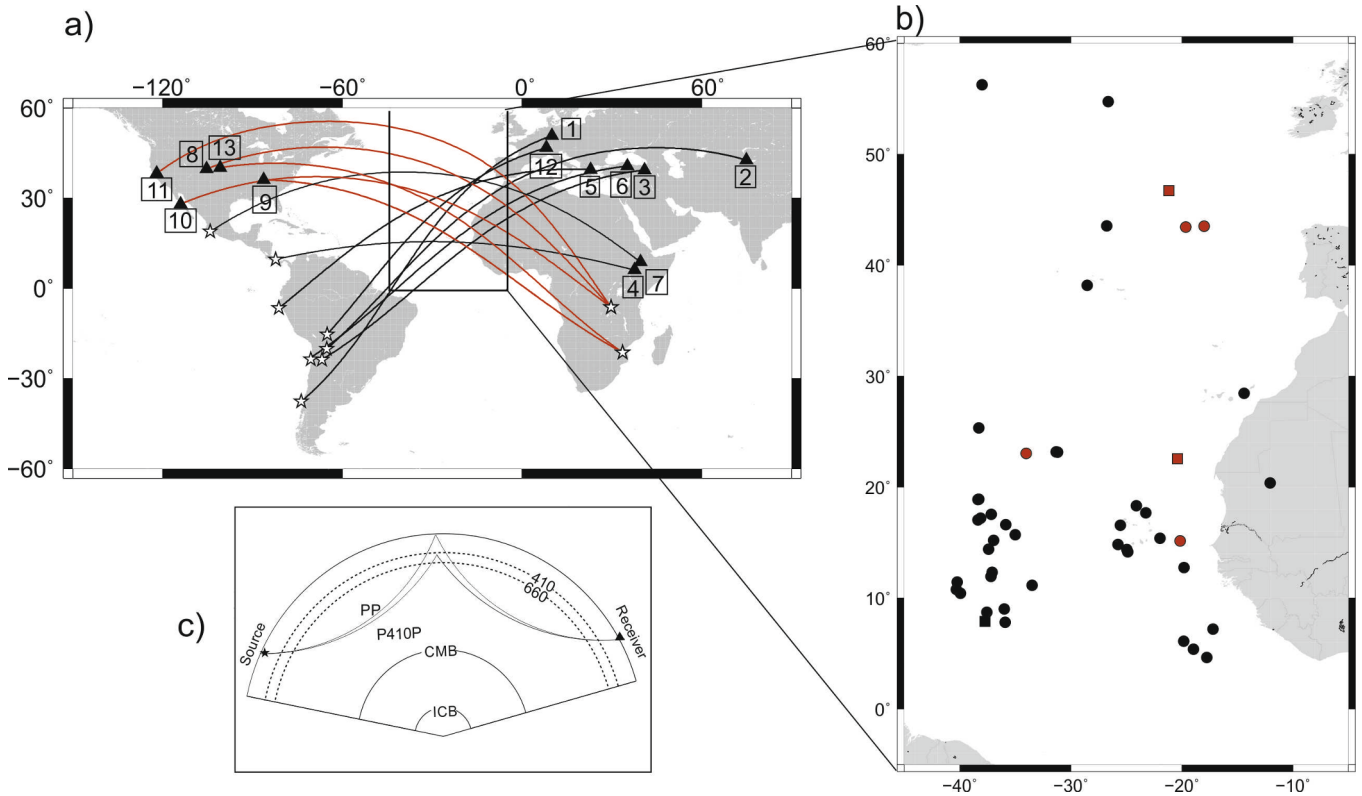

Fig. 1. Investigation area. (a) source-receiver combinations used in this study. Stars denote source regions and triangles indicate the central station of the networks. The numbers on the map are array numbers as given in Table 2. The great circle path is shown by the black line for the source-receiver combinations in SW-NE direction and red line for the ones in NW-SE path. (b) Location of underside reflections at the 410 km discontinuity used in this study for PP precursors (circles) and SS precursors (squares). Black and red circles/squares are compatible with the black and red great circle paths in part (a), respectively. Note that we find a number of crossing paths for similar regions. (c) Example ray paths of the PP and $P^{410}P$ wave reflected off the 410 km discontinuity. CMB: core mantle boundary, ICB: inner core boundary. (For interpretation of the references to colour in this figure legend, the reader is referred to the web version of this article.)

Table 1
Events with visible precursors for PP/SS at the 410 km discontinuity. Net is the network number listed in Table 2. St represents the number of stations for each earthquake. Local-backazimuth and epicentral distance of each event are found in columns 9 and 10, respectively. Event details are from NEIC (National Earthquake Information Centre). H gives the depth of the earthquake. Filt shows the best filter used for each single event and are numbered as follows: 1) bp 5–20 s. 2) bp 5–60 s. 3) bp 6–50 s. 4) bp10-20 s. 5) bp 10–30 s. 6) bp 10–100 s. 7) bp 20–50 s. 8) lp 10 s. 9) lp 20 s. 10) lp 30 s.

Date	Time	Lat	Lon	H (km)	M_W	Net.	St.	Local_Baz.	Epi_dist.	Filt.
1995/08/02	00:14	-23.23	-70.68	33	6.0	1	22	219.266	102.15	7
1997/01/23	02:15	-22.00	-65.72	276	7.1	1	22	218.26	98.21	8
2000/05/12	18:43	-23.75	-66.70	225	7.2	1	21	218.95	87.66	9
2000/12/20	11:23	-39.01	-74.66	11	6.4	1	28	214.93	115.9	10
2003/06/20	13:30	-30.61	-71.64	33	6.8	1	25	217.14	93.2	9
2004/05/03	04:36	-37.69	-73.41	21	6.6	1	27	215.052	114.6	3
2006/04/30	19:17	-27.02	-71.02	12	6.7	1	22	218.48	105.72	9
2007/11/20	17:55	-22.92	-70.48	15	6.1	1	34	219.48	102.09	9
2009/04/17	02:08	-19.58	-70.48	25	6.1	1	32	221.21	99.48	9
2009/11/13	03:05	-19.39	-70.32	27	6.5	1	26	221.28	99.07	9
2010/07/14	08:32	-38.07	-73.31	22	6.6	1	32	211	115.19	10
2011/01/02	20:20	-38.35	-73.33	24	7.2	1	34	213.02	115.42	8
2011/02/11	20:05	-36.42	-72.96	26	6.9	1	31	211.44	113.23	10
2011/06/01	12:55	-37.58	-73.69	21	6.3	1	30	211.255	114.8	8
2012/03/25	22:37	-35.20	-72.22	40	7.1	1	25	215.85	111.75	9
2012/05/28	05:07	-28.04	-63.09	586	6.7	1	28	215.75	102.06	5
2013/10/31	23:03	-30.29	-71.52	27	6.6	1	22	217.40	107.97	9
1995/01/19	15:05	5.05	-72.92	17	6.5	2	7	234.68	124.28	3
2000/09/28	23:23	-0.22	-80.58	23	6.6	2	7	227.83	132.37	1
2003/04/27	22:57	-8.19	-71.59	560	6.0	2	9	230.04	135.01	1
2003/07/27	11:41	-20.13	-65.19	345	6.0	2	10	231.33	139.73	2
2006/09/12	13:30	-28.87	-68.83	114	5.9	2	10	229.94	147.89	2
1999/11/30	04:01	-18.91	-69.14	125	6.6	3	25	233.34	117.15	3
2000/04/23	09:27	-28.31	-62.99	608	6.9	3	21	229.241	117.59	2
2000/05/12	18:43	-23.75	-66.70	225	7.2	3	17	231.70	117.94	5
2000/06/16	07:55	-33.88	-70.09	120	6.4	3	17	227.96	125.62	8
2001/07/07	09:38	-17.53	-71.93	14	7.6	3	20	245.221	118.05	8
2001/04/09	09:00	-32.67	-73.11	11	6.7	3	21	229.004	127.32	5
2001/06/26	04:18	-17.74	-71.34	33	6.8	3	20	235.006	118.19	9
2001/11/09	00:47	9.64	-82.30	10	6.1	4	20	272.118	118.4	8
2009/02/09	14:09	-6.56	-81.15	15	6.0	5	32	238.59	104.00	8
2006/10/20	10:48	-13.46	-76.67	23	6.7	6	32	235.28	115.04	8
2006/10/26	22:54	-13.32	-76.73	28	6.0	6	33	235.29	115.00	6
2007/11/17	17:54	-23.06	-70.59	15	5.9	6	26	230.108	115.81	9
2007/11/20	17:55	-22.92	-70.48	15	6.1	6	26	230.90	115.65	8
2007/12/13	05:20	-23.02	-70.48	16	6.0	6	25	230.96	115.78	5
2008/02/04	17:01	-20.17	-70.04	35	6.4	6	33	231.775	114.20	10
2003/01/22	02:06	18.89	-104.08	27	7.5	7	12	276.72	134.8	5
2005/12/05	12:19	-6.25	29.77	17	6.7	8	39	124.66	117.39	5
2006/02/22	22:19	-21:32	33.58	11	7.0	9	11	123.33	128.11	6
2005/12/05	12:19	-6.25	29.77	17	6.7	10	9	106.878	137.51	5
2005/12/05	12:19	-6.25	29.77	17	6.7	11	25	126.13	137.72	6
2010/03/04	22:39	-22.23	-68.33	114	6.3	12	20	220.27	97.09	1
2011/11/22	18:48	-15.36	-65.09	549	6.6	12	27	221.737	89.9	3
2006/02/22	22:19	-21.324	33.58	11	7.0	13	72	157.466	153.65	10

660 km boundaries (e.g., Courtier and Revenaugh, 2007; Jasbinsek and Dueker, 2007; Thomas and Billen, 2009) indicate that these models are a simplification of Earth structure for the transition zone. Furthermore, Cobden et al. (2008) showed that 1-D reference velocity models such as PREM and AK135 are strongly influenced by different components of a 3-D mantle and do not correspond to a specific physical structure as a consequence.

Previously, it has been suggested that a mantle model with constant chemical composition – pyrolite- and a temperature profile following an adiabat with a potential temperature of 1300 °C agrees well with the observed seismic velocities (e.g., Weidner, 1985; Ita and Stixrude, 1992; Jackson and Rigden, 1998). However, further studies have shown that it is difficult to reconcile the simplest possible 1-D physical model, 1300 °C adiabatic pyrolite with seismic observations. These later studies attempted to define a physical one-dimensional model for the mantle corresponding to the 1D seismic reference models (e.g., Deschamps and Trampert, 2004; Cammarano et al., 2005a,b; Cobden et al., 2008,2009). These physical reference models are based on thermodynamic modelling of mineral physics data compared with different seismic data sets and showed considerable differences compared to 1300 °C adiabatic pyrolite model, in particular near the mantle transition zone boundaries. For instance, Cobden et al. (2008) found models which attain higher velocity gradients between 250 and 350 km depth, higher velocity gradients in the lower transition zone and higher average velocities immediately beneath the 660 km discontinuity, than 1300 °C adiabatic pyrolite model. Furthermore, Xu et al. (2008) showed that a mechanical mixture of basalt and harzburgite matches 1-D seismological models of the transition zone significantly better than the equilibrium assemblage of pyrolitic composition. Despite having an acceptable fit of 1-D physical models to global average seismic data, they cannot account for some of the observations of reflected waves from the transition zone boundaries.

In previous studies, polarities not consistent with the velocity and density jumps of the 410 km discontinuity have been observed in several regions: beneath the Kuriles (Schmerr and Thomas, 2011), beneath the Tasman and Coral Seas (Courtier and Revenaugh, 2007), in the northern Rocky mountains (Jasbinsek and Dueker, 2007) and some parts of SW Pacific (Thomas and Billen, 2009). The observations of polarity changes have been usually interpreted as a melt layer at the top of the mantle transition zone or metastable olivine wedges (e.g.,

Jasbinsek and Dueker, 2007; Schmerr and Thomas, 2011). However, the non-pyrolitic models (e.g., Cobden et al., 2008; Xu et al., 2008) may also potentially explain some polarity observations of the precursory signals. Opposite polarities of PP precursors to the main phase (PP) do not seem to relate to any specific region and reflection points nearby sometimes show opposite polarities. These observations led us to inspect our dataset of PP and SS precursors used in Saki et al. (2015) and try to find a cause for these polarity reversals in PP/SS precursors. A polarity reversal of reflected waves from the underside of the 410 km boundary would require an impedance drop with increasing depth and may therefore provide valuable information for our understanding of dynamic processes at depth. This study also indicates the usefulness of waveform polarities of PP and SS underside reflections for interpreting the thermochemical structure of the upper mantle.

2. Data and processing

We use data downloaded from the Incorporated Research Institute for Seismology (IRIS) including events at distances of 80 to 150 degrees for P waves and 115 to 150 degrees for S waves that have reflection points beneath the Atlantic Ocean. An initial dataset of approximately 1700 broadband seismograms was chosen that included events with M_w greater than 5.8 but without depth limitation, collected from 46 broadband seismic networks including both temporary and permanent deployments. Seismograms of each event were visually inspected to determine the quality of the PP/SS signal. A noise window of 55 s length up to 35 s before the diffracted P/S arrival and a signal window of 50 s length around PP/SS wave were picked to estimate the signal to noise ratio. Only events with a signal-to-noise ratio higher than 3 were retained, which lead to 45 events (Table 1) as the final dataset recorded at one or more of 13 networks (Table 2). Note that the majority of our events have a much higher signal-to-noise ratio than 3. Source-receiver combinations, reflection points and great circle paths are shown in Fig. 1.

The final dataset includes source-receiver locations that define two main directions. The first and dominant propagation path is SW-NE direction. The earthquakes that occurred in South America and were recorded in Eurasia provide the largest number of data for this path. The second source-receiver group are events from Africa recorded in North America, presenting a SE-NW propagation path. The existence of such crossing ray paths allows a better resolution of the discontinuities and may allow us to discriminate between different causes for polarity reversals.

We applied a range of filters to the data in order to find the frequency range where the PP/SS wave and associated precursory signals are the most visible. The bandpass-filtered data with corner periods between 6 and 50 s, 10 and 30 s, as well as lowpass-filtered data with a corner period of 20 s provide us with a clear PP arrival and their precursors but the best filter varies from event to event and is given in Table 1. When $P^{410}P/S^{410}S$ arrivals were detected, we improved the visibility of the precursory signals in order to determine the polarity. To increase the signal-to-noise ratio of the waves we applied two further steps of processing including calculating the Hilbert transform and taking the derivative of the seismic records. The Hilbert transformation applies a $\pi/2$ shift to the phase of the signal (e.g., Rychert et al., 2012). Our approach is comparable with data processing done by Chambers et al. (2005). The further processing step includes computing the wavelet derivative which generates a higher frequency version of the signal and makes onsets of waves clearer. The joint use of Hilbert transformation and derivative operator provides an increase in resolution of the precursor arrivals particularly for the noisy data (see Figure S1) and therefore allows us to identify the polarity of the arrivals with a higher certainty.

Due to the small amplitudes of the precursor signals compared to those reflected from the surface (e.g., Flanagan and Shearer, 1998, 1999; Deuss, 2007, 2009; Schmerr and Garnero, 2007; Schmerr and Thomas, 2011; Lessing et al., 2015; Saki et al., 2015; Reiss et al., 2017), array seismology methods (see Rost and Thomas, 2002, 2009; Schweitzer et al., 2002) were used to further enhance the visibility of the precursor signals. Vespagram and slowness-backazimuth analysis were carried out for each event. While the vespagram approach provides us with the possibility of distinguishing arrivals based on differential slowness and arrival time, slowness-backazimuth analysis is applied to avoid the erroneous picking of any scattered or out-of-plane reflection as the real precursor signal (e.g., Rost and Thomas, 2009) (Figure S2). However, it should be noted that the slowness deviation up to $\pm$ 0.5 s/deg (Rost and Weber, 2002; Rost et al., 2008) from the predicted slowness value of PP/SS was considered to accommodate for array mislocation (e.g., Krüger and Weber, 1992; Jacobeit et al., 2013). For the deep events (depths greater than 90 km) in our dataset, we calculate the traveltimes of possible depth phases using AK135 (Kennett et al., 1995). These depth phases could coincide with the precursors from upper mantle discontinuities and to avoid erroneously picking depth phases instead of precursors, we ignore events when there is no

Table 2
Seismic networks used to compare the polarity and amplitude of PP/SS wave to $P^{410}P/S^{410}S$ wave. Latitude and longitude are given for the central station of each network/array. The number of the array is used in Fig. 1.

#	Network	Latitude [deg N]	Longitude [deg E]	Organisation/Funding
1	Gräfenberg Array (GRF) and German Regional Seismic Network (GRSN)	50.82	10	Bundesanstalt für Geowissenschaften und Rohstoffe
2	Kyrgyz Seismic Telemetry Network	42.66	74.95	Scripps Institution of Oceanography, Kyrgyz Institute of Seismology, Institution of the Russian Academy of Sciences, Joint Institutes for high Temperatures RAS
3	Eastern Turkey Seismic Experiment	39.37	40.99	Kandilli Observatory, Earthquake Research Institute (KOERI), Atatürk University, Cornell University
4	Ethiopia/Kenya Broadband Seismic Experiment	6.07	37.56	Penn State University
5	MEDUSA Multidisciplinary Exp for Dynamic Understanding of Subduction under the Aegean	39.49	22.96	MIT, USC, the University of Athens, Universita di Roma TRE, IPG Paris, INGV Rome, and the National Observatory of Athens
6	North Anatolian Fault	40.69	35.24	Institute of physics of Earth of Russian Academy of science
7	Ethiopia-Afar Geoscientific Lithospheric	8.75	39.55	Grant number: NER/A/S/2000/01003 (Maguire et al., 2003)
8	United States National Seismic Network	39.70	-105.37	ANSS Backbone of the USGS/NEIC and USGS/ASL and Earthscope project of IRIS
9	Cooperative New Madrid seismic Network	36.09	-86.33	St. Louis University/Memphis state, Unites States of America
10	NARS-Baja Seismic Network	28.01	-114.01	University of Utrecht, Netherlands CICESE, Ensenada, Mexico Caltech, Pasadena, United states of America
11	Berkeley Digital Seismograph Network	38.20	-121.94	University of California, Berkeley, CA, United States
12	Switzerland Seismological Network	46.76	8.15	Swiss seismological service
13	USArray Transportable Array (NSF Earthscope Project)	40.125	-100.79	IRIS Transportable Array (IRIS_TA)

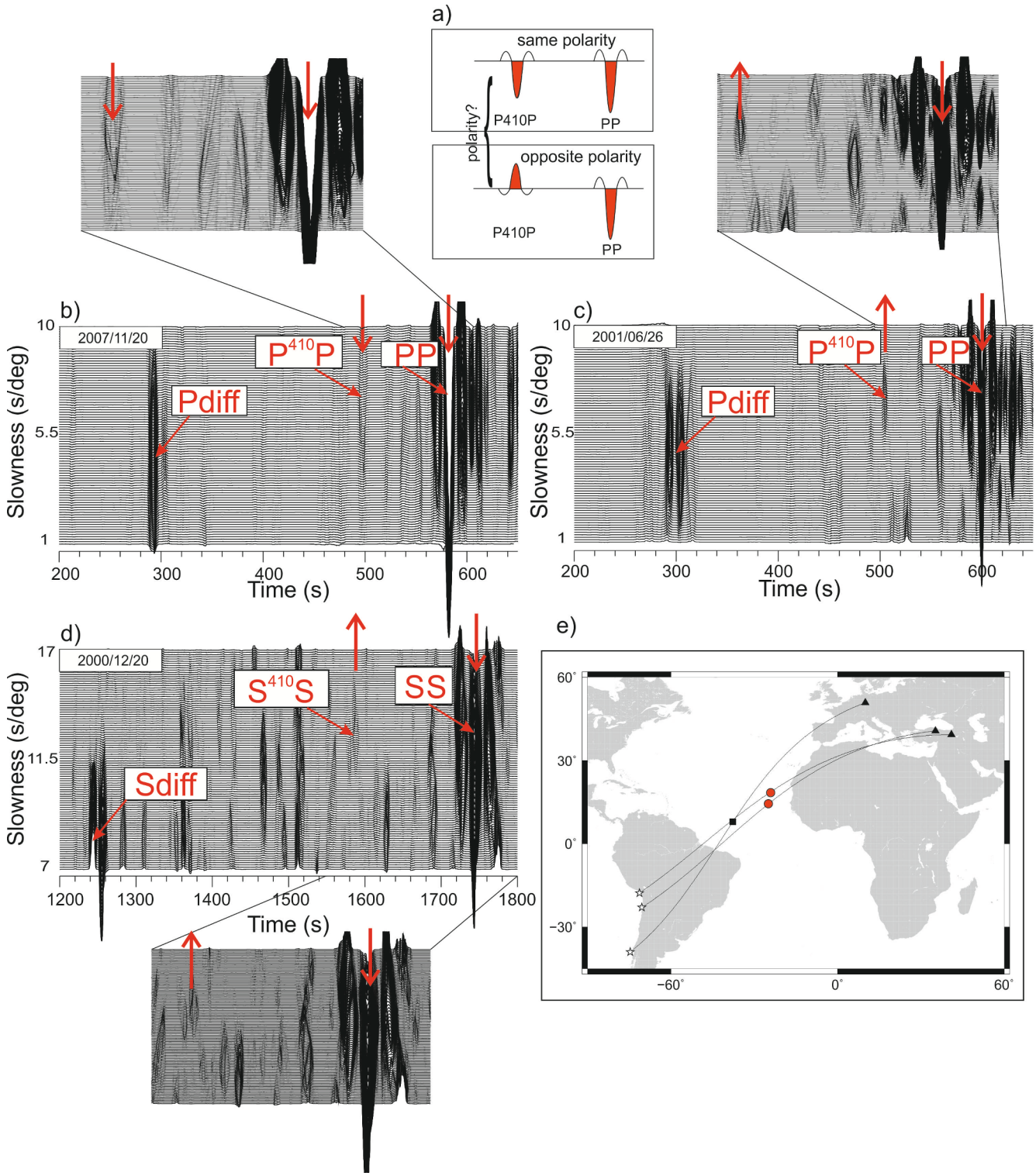

Fig. 2. Comparison of the polarity behaviour of the PP/SS and $P^{410}P/S^{410}S$ phases. (a) Cartoon illustrating the "same polarity" and "opposite polarity" definition for PP or SS and associated precursor used in this study. Note that PP and the precursors are not to scale for better visibility. (b) Example of "same polarity" observation for P wave in the vespagram for event 20-NOV-2007 recorded at array number 6 (see Table 2). (c) 4th root vespagram of an "opposite polarity" observation of P wave for event 26-JUN-2001 recorded at array number 3 (Table 2). (d) Example of "opposite polarity" observation of S wave in the vespagram for event 20-DEC-2000 recorded at array number 1 (Table 2). All events are low-pass filtered with a corner period of 20 s. The insets show the enlarged window including the PP/SS and $P^{410}P/S^{410}S$ waves for each vespagram. (e) Map showing great circle paths for the events in part (b), (c) and (d). The red circles indicate the reflection points for the source-receiver path for PP precursors and the black square represents those of SS precursor. (For interpretation of the references to colour in this figure legend, the reader is referred to the web version of this article.)

clear separation between the two. This approach was described by Schmerr and Thomas (2011).

We extracted polarity information of all precursor arrivals ($P^{410}P$/$S^{410}S$) and the main phase (PP/SS) for each 4th root vespagram, created from Hilbert transformed and derivative of the seismic data and compared them separately for every event. If the underside reflection from the 410 km discontinuity ($P^{410}P$/$S^{410}S$) showed the same polarity as the PP/SS phase, we called it a "same polarity" observation and in the case of inverted polarity we marked them with "opposite polarity" (Fig. 2.a). Fig. 2 shows two examples indicating "same polarity" and "opposite polarity" for PP and $P^{410}P$ waves. These two earthquakes are selected from two different source-receiver combinations with similar propagation path in SW-NE direction. The vespagrams show clearly separated PP precursors from other arrivals such as Pdiff coda waves. Previous studies showed a number of interfering phases (i.e., PKiKP) that may arrive in the time and distance window of the PP precursors (e.g., Shearer, 1991; Flanagan and Shearer, 1998; Lessing et al., 2015) and may influence the precursor arrivals. Since array stacking techniques allow identification of different arrivals based on their slownesses and we only used very clear examples in this study, we therefore believe that our observations of polarity behaviour are robust and are not influenced by interfering phases.

We found only very few S-wave precursors in our dataset compared to P-data precursors (Saki et al., 2015). The precursors to SS wave were mostly absent in the vespagram or in some cases distorted by interference of other phases (Figure S3). We avoided including any doubtful polarity observations in our results. One example of "opposite polarity" behaviour of $S^{410}S$ and SS waves is provided in Fig. 2. Applying these processing steps to each event provides a map of polarity observations beneath the whole Northern Atlantic. The polarity observations of the three S waves all showed the "opposite polarity" behaviour. Due to the sparse distribution of the S wave reflection points and to avoid a complicated map of polarities, we chose to create a polarity map for the P wave observations only. However, the results of the polarity behaviour of the S wave will be discussed in section 4 in combination with P wave observations.

3. Results

3.1. Polarity observations

We divided the polarity observations of P wave into two different categories: for the majority of the events, due to the high signal to noise ratio, the polarity of the main phase (PP) and corresponding precursory signal are easily distinguishable and can be easily compared while for the rest of the dataset the complexity of either the PP wave or the precursor arrival waveforms made a clear polarity determination difficult. To those cases we attributed the second order of importance and marked them by "possibly same" or "possibly opposite" polarities.

We find a large number of "same polarities" for $P^{410}P$ wave compared with the PP waves but there is also a considerable number of opposite polarity observations. The polarities found in our dataset reveal a complicated behaviour in this region (Fig. 3). While most of the "same polarity" observations are concentrated in southwest of the investigation area (Fig. 3a) we detect other groups of events with the "same polarity" behaviour scattered over the investigation area. There are also a few points with "opposite polarity" in the southwest. Most observations in the north of the area seem to have "opposite polarity" behaviour but some events exhibit the same polarity in this region. As there is not a clear regional dependence of observed polarities we conclude that regional variations may not be the only cause for polarity reversals. However, a limiting factor for this assumption is the uneven distribution of the reflection points, especially in the northern part of our study area, where only a few 410 km discontinuity reflections are found.

Since polarity changes of reflected waves can arise from seismic anisotropy if waves travel in different directions (e.g., Thomas et al., 2011; Saki et al., 2018), we investigated the dependence of observed polarities on the local backazimuth with many events in the southwest of the investigation area and but only few points in the north. The existence of "same polarity" behaviour for the events propagating along crossing paths (blue circle in Fig. 3b) as well as events displaying different polarity behaviour despite having a similar propagation path (red circle in Fig. 3b), lead us to revoke the hypothesis of local backazimuth dependence of observed polarities as the sole contribution for variable polarities.

Polarity observations are sorted according to the epicentral distance of the events (see Table 1) as shown in Fig. 3. A comparison between the observed polarities and the epicentral distance of the earthquakes reveals that polarity of PP precursors seems to depend on the epicentral distance. The events with epicentral distances greater than 118 degrees mostly show "opposite polarities", while for those with smaller epicentral distances, the "same polarity" is dominant (Fig. 3c, d). The display of same and opposite polarity observations (as well as possibly same and possibly opposite polarities) over distance indicates that the transition is not sharply defined but there seems to be a large preference for a transition between the two different polarity behaviours at around 118 degrees epicentral distance (Fig. 3d).

3.2. Reflection coefficient modelling

A measure of the amplitude and polarity of the reflected and transmitted waves is expressed by the reflection coefficient which strongly depends on the impedance (i.e., product of density and velocity) contrast of the two media above and below the interface as well as the incidence angle and can be calculated using the Zoeppritz's equations (Zoeppritz, 1919). The perturbations in temperature and chemical content of the mantle minerals may produce observable changes in impedance contrast. We compute the values of the reflection coefficients of PP and $P^{410}P$ wave for various input 1-D seismic structures (Fig. 4) and compare them with our polarity observations. In each calculation, the angle of incidence at the discontinuity varies from zero, where the wave is propagating perpendicular to the interface, to 90 degrees, where the wave is travelling parallel to the boundary. It should be noted that each angle of incidence can be translated into an epicentral distance value but these vary for different reflection depths. We calculated the epicentral distance associated to each angle of incidence using the Taup toolkit (Crotwell et al., 1999).

To calculate the reflection coefficients, values of density, P and S wave velocities for the two layers above and below the 410 discontinuity are required. We first do this for a 1-D seismic reference model, AK135 (Kennett et al., 1995) and a mineralogical model, pyrolite (Sun, 1982). We used the thermodynamic modelling code Perple_X (Connolly, 1990, 2005), together with the mineral thermoelastic parameter database of Stixrude and Bertelloni (2011) and equation of state of Stixrude and Bertelloni (2005) to predict the seismic properties (V_P, V_S and density) of pyrolite. These parameters and equation of state were derived within the same thermodynamic framework and are therefore internally consistent.

The temperature gradient follows an adiabat (defined as the locus of constant entropy, given by Perple_X), with a potential temperature of 1300 °C where the "potential temperature" is the temperature that the adiabat would reach if extrapolated along the adiabat to the Earth's surface. The pyrolite model we use is based on the study of Sun (1982) and has the following composition, expressed in molar percentages of oxides: 3.25% CaO, 6.24% FeO, 49.13% MgO, 2.77% Al_2O_3 and 38.61% SiO_2 (the equivalent composition in weight% would be: 3.5% CaO, 8.6% FeO, 38.0% MgO, 5.4% Al_2O_3 and 44.5% SiO_2). Reflection coefficients for AK135 and this pyrolite model are shown in Fig. 4.

A comparison between the reflection coefficients of the PP and $P^{410}P$ waves reveals that the polarity is supposed to be the same over the whole distance range in our dataset. This is true for both tested

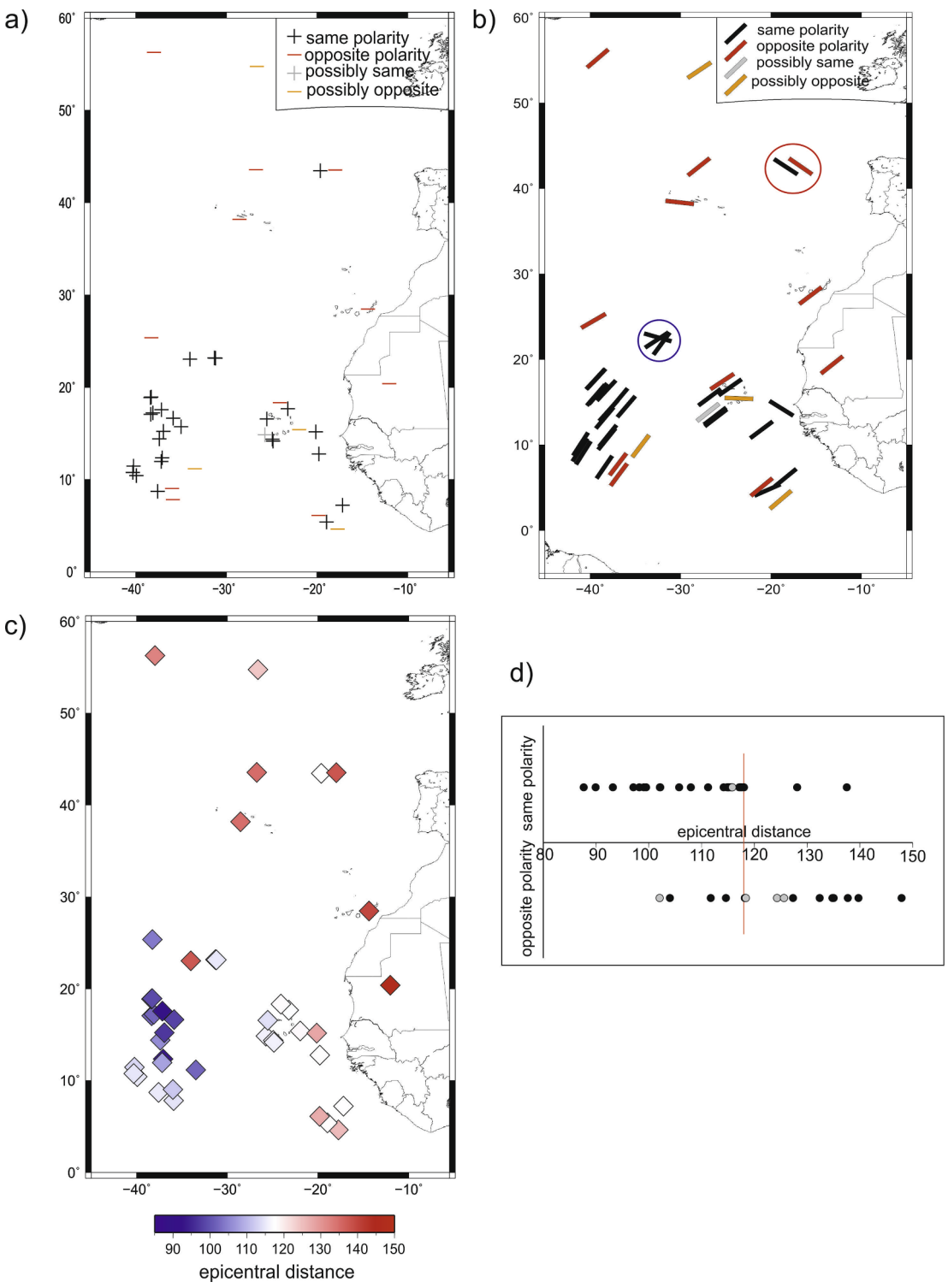

Fig. 3. (a) Map of polarity observations of P wave displayed at the location of each reflection point of the data. (b) Map of observed polarities shown as colour information and oriented according to the local backazimuth of each reflection point, at the midpoint between the source and receiver. For each reflection point the local backazimuth is measured clockwise as the angle between North and the direction towards the epicenter. The red circle marks events with different polarity behaviour despite travelling in the same direction and the blue circle indicates the reflections showing the "same polarity" observations with crossing propagation paths. (c) Colour coded epicentral distance for each event displayed at the corresponding reflection point of each earthquake. (d) "Same" and "opposite" polarity observations versus epicentral distance of the corresponding event. The vertical red line is associated with epicentral distance of 118 degrees. Grey circles represent "possibly same" and "possibly opposite" polarities.

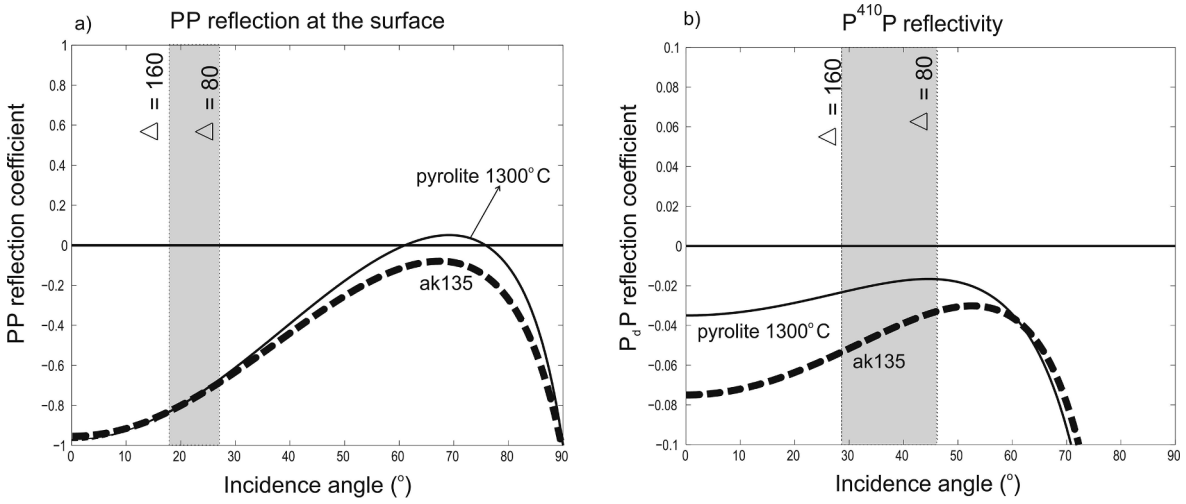

Fig. 4. Comparison of reflection coefficients of (a) the PP wave reflected at the surface and (b) the $P^{410}P$ wave reflected off the underside of the 410 km discontinuity for the two velocity models of AK135 (dashed line) and 1300 °C adiabatic pyrolite (solid line). The epicentral distance corresponding to the different incidence angles at the surface and at the 410 km boundary for the data set are shown by the grey-dashed area. Comparison of the calculated reflection coefficients in (a) and (b) indicates the "same polarity" behaviour for the entire epicentral distance range in our dataset.

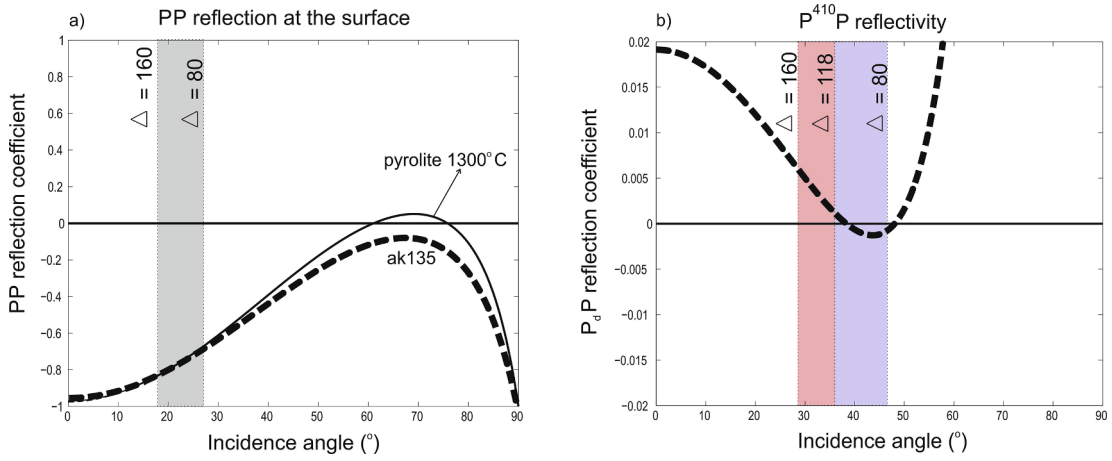

Fig. 5. (a) Reflection coefficient of the PP wave at the surface. (b) Example of reflection coefficient at the 410 km discontinuity, which satisfies the criterion of positive reflection coefficient for angle of incidence between 30.51 and 37.53 degrees (pink-shaded area) and negative values for those between 37.53 and 46.77 degrees (blue-shaded area). (For interpretation of the references to colour in this figure legend, the reader is referred to the web version of this article.)

models, although the pyrolite model produces positive reflection coefficients for PP waves for large angle of incidences but negative ones for the precursor, hence potentially leading to a change of polarity. However, this happens only at very short epicentral distances not probed by PP waves (Fig. 4). We therefore tested how the reflection coefficients changed with variations of velocities and densities above and below the 410 km discontinuity to find models that can explain our observations at incidence angles represented in our dataset. One example of such a model is shown in Fig. 5.

We prescribe that the density below the 410 km discontinuity (i.e., wadsleyite-bearing layer) always exceeds the density above the 410 km discontinuity (i.e., olivine-bearing layer) since it is difficult to imagine a scenario where the layer above the phase transition is denser than the one below for long periods of time. V_P and V_S are varied from -10% to +10% of the initial values of both AK135 and the pyrolite model. This produces 720 million combinations of density, compressional and shear wave velocity for two layers and we search for all possible combinations of density, P and S wave velocities which satisfy the criterion of showing positive reflection coefficients for $P^{410}P$ wave for incidence angles in range of 30.51 to 37.53 degrees (epicentral distance range of 118 to 150 degrees) and negative values for the incidence angles between 37.53 and 46.77 degrees (epicentral distance range of 80 to 118 degrees) (Fig. 5).

The values of density, compressional and shear wave velocities of the two layers that produce reflection coefficients which fit our polarity observations are shown in Fig. 6 for the pyrolite model at 1300 °C (for AK135 see Figure S4). The obtained models exhibit a velocity decrease for P and S waves across the 410 km discontinuity. The density jump at 410 km depth, however, is smaller than pyrolite but still positive, as prescribed. The calculated change in both compressional and shear wave velocities across the discontinuity is up to minus 13% but mostly falls within the range of minus 3–4% and minus 5–7% for P and S wave velocities, respectively (Fig. 6).

4. Discussion

Our polarity observations indicate that the reference Earth model AK135 is not capable of explaining the polarity behaviour of all underside reflections from the 410 km discontinuity ($P^{410}P$). Also petrologically-predicted mantle models such as pyrolite at 1300 °C fail to predict all the variations in polarity that we see in our data, especially for the opposite polarity behaviour of $P^{410}P$ with respect to PP waves. For these models the same polarity of the underside reflections compared with PP would be expected for the entire distance range where PP

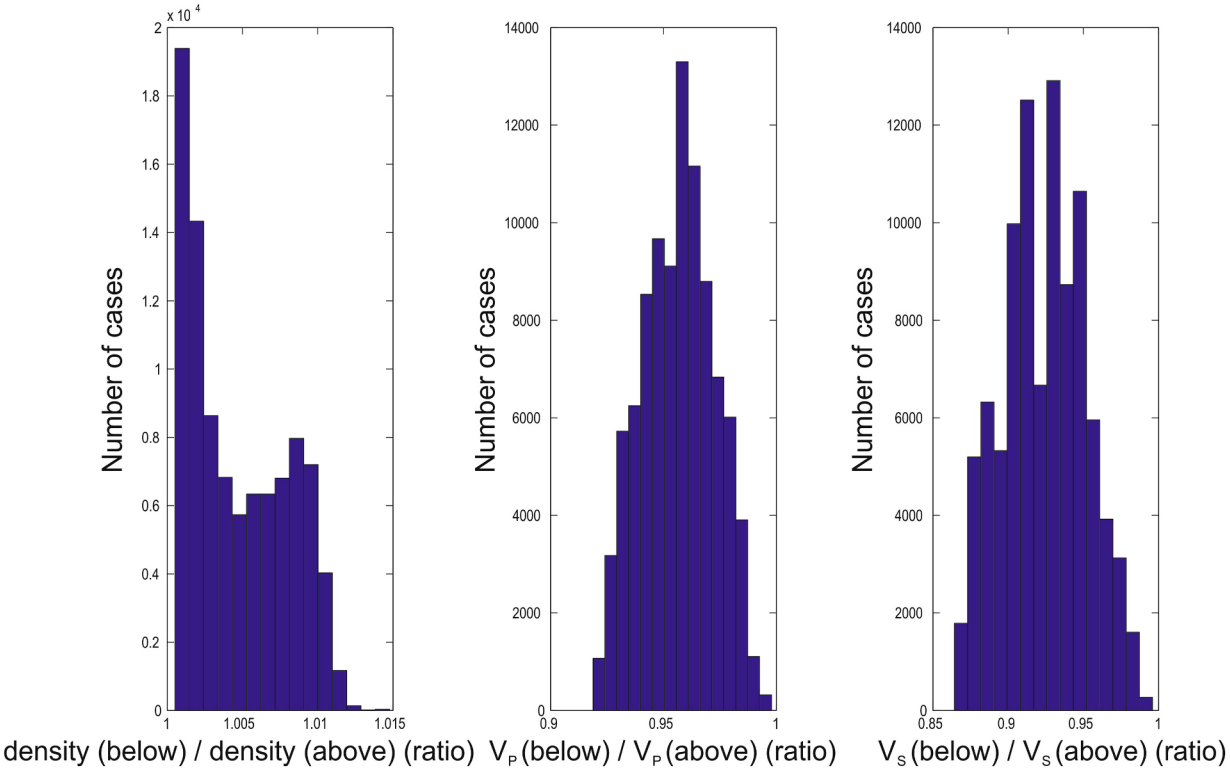

Fig. 6. 2-D histograms of the density, compressional and shear wave speed ratios (Vp, Vs) of the wadsleyite-bearing (bottom layer) to olivine-bearing (top layer) layer for all the cases that match the polarity observation in the dataset. The reduction in Vp and Vs reaches 13% but mostly falls within the range of 3–4% and 5–7% for P and S waves, respectively.

and SS precursors are visible. Our results clearly show that this is not always the case, and similar observations of polarity changes have been observed in other studies (e.g., Courtier and Revenaugh, 2007; Jasbinsek and Dueker, 2007; Thomas and Billen; 2009; Schmerr and Thomas, 2011). In those publications no clear pattern or regional dependence could be associated with the polarity changes of the $P^{410}P$ wave.

We do not think that topography is the source for polarity reversals of the PP and SS underside reflections. Lessing et al. (2015) using 2D modelling of upper mantle discontinuity structure and investigating the effect of topography on detection of precursors showed that large-scale discontinuity topography (greater than 30 km) reduces amplitudes but no polarity reversal was reported. Topography leads to travel time changes (e.g., Thomas and Billen, 2009) and focusing and defocusing effects that can create apparent double reflectors (e.g., Zheng and Romanowicz, 2012) but we are not aware that it causes polarity changes.

In our dataset, we find two possible patterns that could cause polarity reversals: a regional change where the northern part of our investigation area shows mostly “opposite polarities” and the southern part shows mostly “same polarities”. This possibility would account for around 80% of our observations. A regional difference in mineralogy could possibly explain this behaviour.

As a second possibility, it seems that the epicentral distance i.e., the angle of incidence at the discontinuity could determine the polarity of the wave: the epicentral distance of 118 degrees (angle of incidence of 37.53 degrees) is the point where the reflection coefficient of $P^{410}P$ wave changes sign. This pattern is consistent with 84% of the observed polarities of $P^{410}P$ wave (Fig. 7). The epicentral distance range of the events with SS precursor observations fall within the range of 115 to 150 degrees. The best-fitting models to our PP wave polarity observations agree with the polarity changes observed for the S waves as well (see Figure S5).

A third possibility could be seismic anisotropy, however, we find events with the same direction of travelling that show opposite polarities of the $P^{410}P$ waves. In other regions, we find same polarities for different travel directions. In addition, Saki et al., (2018) showed that the effect of deformation is only visible at shorter epicentral distance ranges (epicentral distance ~70 degrees) when using published elasticity tensors of wadsleyite and olivine. We therefore disregard this possibility for the observations in our investigation area.

To investigate the possible causes for reducing the impedance contrast so that it fits our observed polarities, and also due to the strong effect of water and iron content of the mantle minerals on their elastic properties (e.g., Chen et al., 2002; Mao et al., 2008a,b, 2011; Tian et al., 2012; Thio et al., 2016) we concentrated on two different possibilities: Effect of water and effect of iron.

4.1. Effect of water

Transition zone minerals have different properties compared with upper mantle minerals such as water solubility (Williams and Hemley, 2001) and electrical conductivity (e.g., Xu et al., 1998). Water in the mantle may modify the properties of the phase change at 410 km depth (Wood, 1995; Helffrich, 2000; Chen et al., 2002; van der Meijde et al., 2003; Mao et al., 2008a,b) including promoting partial melting (Hirschmann, 2006) and altering rheological and elastic properties (e.g., Chen et al., 1998; Huang et al., 2005; Jacobsen and Smyth, 2006; Karato, 2006).

Based on high-pressure mineral physics studies, the transition zone minerals have high water solubility on the order of 1–3 wt.%, while this tendency in water absorption reduces to less than 0.1–0.2 wt.% for the minerals in the upper mantle (Kohlstedt et al., 1996; Bolfan-Casanova et al., 2000; Saal et al., 2002; Hirschmann, 2006). Since both ringwoodite and wadsleyite have a large water storage capacity, they provide a possibility of containing a large water reservoir in the mantle

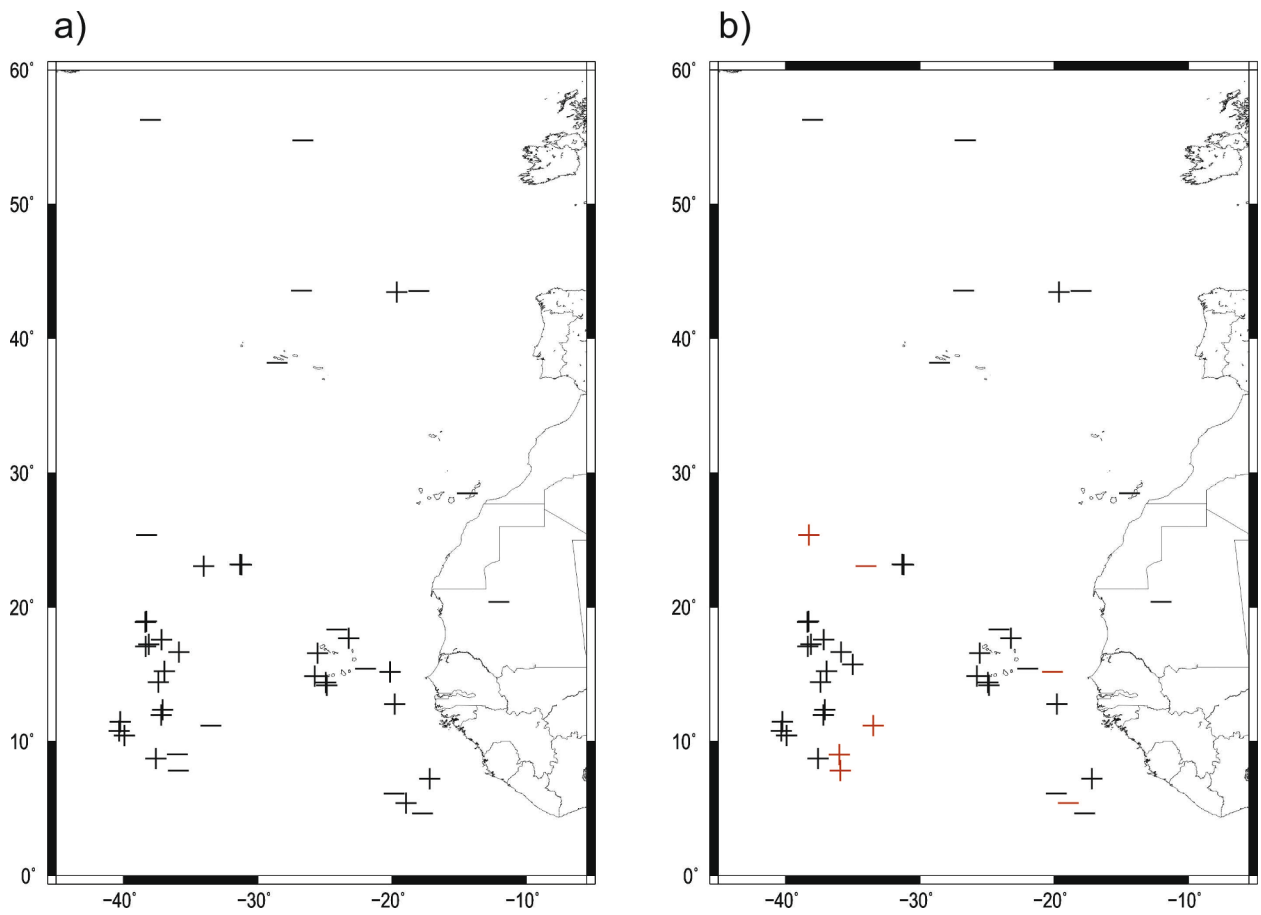

Fig. 7. Comparison of (a) polarity observations in our dataset and (b) predicted polarities from synthetic modelling displayed at location of the reflection point for each event. Red symbols in (b) represent the predicted polarities which are not in agreement with polarity observations in the data.

transition zone (Smyth, 1994; Pearson et al., 2014). This may result in separating the wet mantle transition zone from the dry minerals above and below, the so-called "transition zone water filter" suggested by Bercovici and Karato (2003). However, despite a high storage capacity of water of transition zone minerals, the actual amount of water in the mantle transition zone is still unknown. A recent study using Ice-VII inclusions in diamond shows that water-rich fluid occurs in regions within the transition zone depths and around the 660 km boundary, or possibly in shallower lower mantle (Tschauner et al., 2018).

One interpretation of polarity reversals presented in the literature is melt at the top of the 410 km boundary (e.g., Courtier and Revenaugh, 2007; Jasbinsek and Dueker, 2007; Thomas and Billen; 2009; Schmerr and Thomas, 2011) which could be due to dehydration of the water-rich minerals of the mantle transition zone (on transforming to upper mantle minerals with a lower water storage capacity) or metastable olivine wedges. Existence of a low-velocity zone near the 410 km discontinuity, which would support this hypothesis, has been documented in regional (e.g., Revenaugh and Sipkin, 1994; Vinnik and Farra, 2002; Vinnik et al., 2003; Courtier and Revenaugh, 2007; Jasbinsek and Dueker, 2007; Bagley et al., 2009; Jasbinsek et al., 2010; Schmandt et al., 2011; Bonatto et al., 2015; Morais et al., 2015; Thompson et al., 2015; Liu et al., 2016; Wei and Shearer, 2017) and global scale studies (e.g., Vinnik and Farra, 2007; Tauzin et al., 2010) and is supported by experiments as well (e.g., Freitas et al., 2017). Our observations of polarity reversals require a negative velocity contrast when crossing the 410 km discontinuity from above, a melt layer atop the 410 km boundary is therefore not compatible with our observations, since it would lower the velocity above 410 rather than below.

To further investigate the effect of water on the amplitude and polarity of the P and S wave reflections off the 410 km discontinuity beneath the Northern Atlantic we tested a range of pyrolite models with 1 wt.%, 2 wt.% and 3.3 wt.% water in wadsleyite. This is compatible with the water filter hypothesis suggested by Bercovici and Karato (2003). The water content is partitioned between olivine:wadsleyite:ringwoodite in the ratios 1:6:3, to reflect their different water storage capacities. Hydrous models are assumed to have pyrolite composition in the major oxides, with substitution of Mg^{2+} or Si^{4+} by H^{+} for the hydration, and they are taken from those published in Thio et al. (2016). Thio et al. (2016) derived 10,000 seismic models for several water contents, in which the fundamental thermoelastic properties (volume V_0, bulk modulus K_{T0}, shear modulus G_0, pressure derivatives dK/dP and dG/dP, Helmholtz free energy F_0 and Debye temperature θ_0) of olivine, wadsleyite and ringwoodite were variable. The ranges of each parameter were defined according to a literature search of the elastic properties and phase relations in hydrous olivine and its high pressure polymorphs as a function of chemical composition (see Thio et al., 2016, for the ranges and input experimental data). All remaining mineral properties were kept the same as in Stixrude and Bertelloni (2005, 2011). It should be noted that we did not correct the wave speeds for anelasticity.

To calculate the average of the V_P, V_S and density of olivine and wadsleyite from 10,000 models derived by Thio et al. (2016), the criterion of phase transformation of olivine to wadsylite occurring between 405 km and 415 km was applied. This leads to the average of ~6000–9000 different hydrous models for olivine and wadsleyite. The number of picked models varied between different hydrous models with 1 wt.%, 2 wt.% and 3.3 wt.% of water. The standard deviations for the averaged values of density, compressional and shear wave velocities

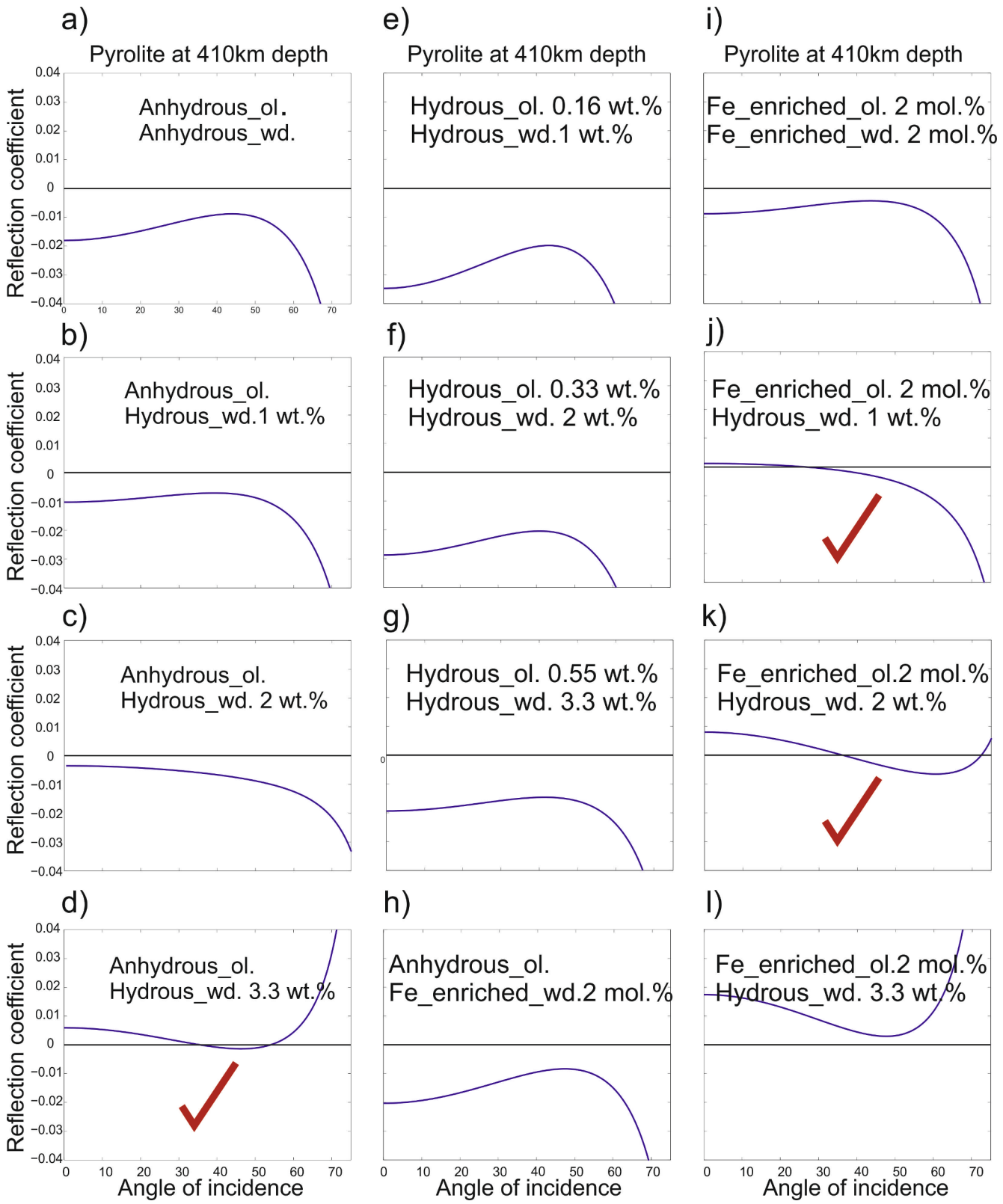

Fig. 8. Calculated reflection coefficients of the $P^{410}P$ wave reflected off the 410 km discontinuity for different concentrations of water and Fe in olivine and wadsleyite using the Zoeppritz equation. Olivine and wadsleyite are abbreviated as ol and wd, respectively. Red tick marks indicate the three different cases of combined hydrous wadsleyite layer with anhydrous or Fe-enriched olivine that fit our P wave polarity observations. (For interpretation of the references to colour in this figure legend, the reader is referred to the web version of this article.)

fall within the range of ± 0.0079 to ± 0.0837 which may not have a considerable influence on the calculated reflection coefficients of the reflected waves. Combination of hydrous/anhydrous olivine and wadsleyite produces 7 different categories for which we show the calculated reflection coefficients of $P^{410}P$ wave reflected off the 410 km boundary in Fig. 8a–g. Most of the hydrous models create a negative reflection coefficient for PP wave reflected at the 410 km depth and at the distance range of 80 to 150 degrees which implies the "same polarity" behaviour (compared to the reflection coefficient of PP wave reflected off the surface, see Fig. 4) and is therefore inconsistent with our polarity observations. However, the combination of anhydrous olivine and 3.3 wt.% water-rich wadsleyite (Fig. 8.d) produces reflection coefficient values which are in agreement with the polarity-distance pattern in our data set and could be considered as one of possible sources of causing polarity reversal of $P^{410}P$ waves. This amount of water in wadsleyite is relatively high but a study by Fei et al. (2017) suggests that the mantle transition zone stores around ~1–2 wt.% water and could be nearly water-saturated on a global scale. Furthermore, Mao et al. (2008b) showed that ~1 wt.% H_2O in wadsleyite at 410 km depth is required in order to reconcile seismic bulk sound velocities with a mantle of pyrolitic composition (although there is no requirement that the bulk mantle composition should be pyrolitic).

Experiments on the elastic properties of olivine and wadsleyite indicate both P and S wave speeds will decrease with increasing water content (e.g., Jacobsen and Smyth, 2006; Thio et al., 2016). Thio et al. (2016) showed the effect of changing water content, temperature and iron content on the average velocities, average densities and velocity and density gradients between 450 and 600 km depth for pyrolitic composition. They observed the reduction of the average value of V_P on the order of ~0.6 ± 0.01%, 1.25 ± 0.02% and 2 ± 0.04% in the case of having ~1, 2 and 3.3 wt.% water, respectively compared to pyrolitic composition with 0 wt.% water and temperature following an adiabat with T = 1573 K. The reduction in V_S shows a larger range of ~1.3% ± 0.01, 2.8 ± 0.02% and 4.4 ± 0.04% in the case of 1, 2 and 3.3 wt.% water. Our observed reduction in both P and S wave velocities from polarities of PP precursors on the order of 3–4% and 5–7%, are higher than the values calculated by Thio et al. (2016). While we focus on the phase transformation of olivine to wadsleyite occurring only at the 410 km discontinuity, Thio et al. (2016) calculated the reduction in V_P and V_S for the average transition zone and this therefore may explain the different values obtained in our study and those from Thio et al. (2016). Nevertheless, the water contents required from our modelling to explain our seismic observations are on the high side and may be too high for Earth conditions.

4.2. Effect of iron

Recent mineral physics experiments on partially hydrated $(Mg, Fe)_2SiO_4$ show that negative gradients of compressional and shear wave velocities cannot arise from hydrogen or H_2O incorporation into olivine and wadsleyite alone (Buchen et al., 2018) and we need an additional source for creating a negative velocity contrast across the 410 km discontinuity. This may offer an alternative to the extremely high water content of 3.3 wt.% in wadsleyite (Fig. 8) required by our hydrous models. Therefore, in search of further scenarios that can explain negative velocity gradients with depth across the 410-km discontinuity we tested iron-enriched models as well. To create the iron-enriched models, we increased the mol. % of FeO in pyrolite by 2% (i.e., to 9.24%) while increasing the amount of all other oxides by 3% so that their relative proportions (i.e., ratios) stay the same.

Wadsleyite in the Earth's mantle is thought to contain ~10% iron (e.g., Ringwood and Major, 1967; Frost, 2003a). The effect of iron on the elasticity of wadsleyite has been studied before (e.g., Sawamoto et al., 1984; Li and Liebermann, 2000; Wang et al., 2014; Thio et al., 2016) and Thio et al. (2016) reported the decrease of average compressional and shear velocities in the transition zone, in the case of increasing the iron content to the pyrolite composition. Furthermore, Tian et al. (2012) benefitting from first-principles simulation at pressures from 0 to 30 GPa, reported a decrease in P and S wave speed by an average of 2.2% and 3.5% respectively for an iron-bearing wadsleyite.

The calculated reflection coefficients of the PP wave at the 410 km discontinuity using Fe-enriched models are shown in Fig. 8.h-l. Based on our results, the two cases of Fe-enriched olivine in combination with water-enriched wadsleyite by 1 wt.% and 2 wt.% can explain our polarity observations. However, such models create a negative density contrast across the 410 km discontinuity (Figure S6), which in a static Earth is not a realistic scenario. In a dynamic Earth, however, density inversions may exist on short time scales. This is a sometimes observed scenario in geodynamic models (U. Hansen, pers. comm).

To gain a more precise estimation of the effect of iron on the P and S wave velocities and density of olivine and wadsleyite we constructed a mineralogical model including the data from high-pressure Brillouin spectroscopy studies on single crystals. We explored the relevant ranges of Fe/(Fe + Mg) in olivine and wadsleyite (up to Fe/(Mg + Fe) of 0.5 and 1.0 mol. %, in wadsleyite and olivine, respectively) for temperature of 1773(+60) K. In the case of olivine, we used properties determined for forsterite Mg_2SiO_4 (Zha et al., 1996) and fayalite Fe_2SiO_4 (Speziale et al., 2004). To correct for the effect of H_2O, we modelled wadsleyite properties based on anhydrous Mg_2SiO_4 (Zha et al., 1997), slightly hydrous $(Mg_{0.89}Fe_{0.11})_{1.98}SiO_{3.96}(OH)_{0.04}$ (0.24 wt.% H_2O, Buchen et al., 2018), and strongly hydrous wadsleyite $(Mg_{0.89}Fe_{0.11})_{1.85}SiO_{3.7}(OH)_{0.3}$ (1.93 wt.% H_2O, Mao et al., 2011). Reported finite-strain parameters were complemented with tabulated thermo-elastic parameters (Stixrude and Lithgow-Bertelloni, 2011) to compute densities and elastic moduli at high pressures and high temperatures for each composition. The compositions were mixed to obtain any desired Fe/(Mg + Fe) ratio for each phase and their properties averaged according to the Voigt-Reuss-Hill scheme (Hill, 1952; Watt et al., 1976).

We mapped all relative contrasts $d\ln X = 200 \times (X_{WA} - X_{OL})/(X_{WA} + X_{OL})$ in sound wave velocities and densities between olivine and wadsleyite as a function of iron distribution and at conditions relevant for the 410-km discontinuity (Fig. 9). Regardless of the assumed temperature, negative gradients in P-wave and S-wave velocities across the olivine-wadsleyite transition are again revealed for extreme iron enrichment in wadsleyite with Fe/(Mg + Fe) in excess of ~0.3. At the same time, however, olivine Fe/(Mg + Fe) ratios need to remain below ~0.1. While wadsleyite compositions can approach the required Fe/(Mg + Fe) ratios at pressures between 12 and 13 GPa, where the wadsleyite stability field extends to higher Fe/(Mg + Fe) ratios (Frost, 2003a; Stixrude and Lithgow-Bertelloni, 2011), they would not be in chemical equilibrium with the required olivine compositions.

Negative compressional and shear wave velocity gradients across the 410 km discontinuity can arise from iron enrichment in wadsleyite (Fig. 9a, b). From an equilibrium thermodynamic point of view, scenarios that lead to negative velocity gradients across the olivine-wadsleyite phase transition cannot be reconciled with the $(Mg, Fe)_2SiO_4$ phase diagram and would require additional processes such as melting at the 410-km discontinuity (e.g., Bercovici and Karato, 2003) to redistribute iron between olivine and wadsleyite. Furthermore, adding iron to wadsleyite would increase the density contrast at 410 km depth (Fig. 9c) while our observations required a smaller contrast than the ones given by a pyrolite model. The addition of iron to wadsleyite therefore appears not to be compatible with our observations on polarity reversals. Instead, iron enrichment above the 410 km discontinuity with, for example, Fe/(Mg + Fe) = 0.3 in olivine and Fe/(Mg + Fe) = 0.1 in wadsleyite would result in a negative density contrast of -2% to -3% (Fig. 9c). In combination with hydration of wadsleyite, this might explain the polarity reversals at epicentral distances around 118 degrees as shown in Fig. 8j and k. Again, such a distribution of iron between wadsleyite and olivine would not follow the phase

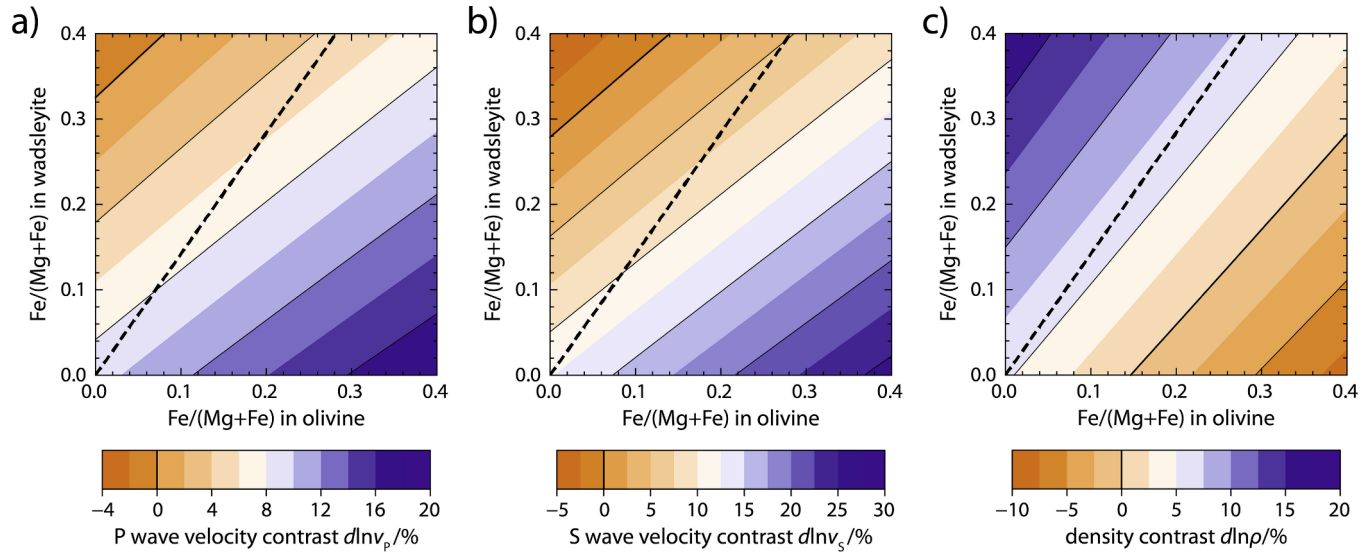

Fig. 9. Contrasts in P wave velocity (a), S wave velocity (b), and density (c) between olivine and wadsleyite at 14 GPa and 1773 K as a function of the Fe/(Mg + Fe) ratio in both minerals. Compositions on the bold dashed line are in mutual chemical equilibrium. Compositions above (below) the bold dashed line require iron enrichment in wadsleyite (olivine) that does not follow equilibrium iron partitioning. Note the negative velocity contrasts for high Fe/(Mg + Fe) in wadsleyite and low Fe/(Mg + Fe) in olivine (upper left corner in a and b). Negative density contrasts result from high Fe/(Mg + Fe) in olivine and low Fe/(Mg + Fe) in wadsleyite (lower right corner in c).

diagram of the $(Mg, Fe)_2SiO_4$ system (Frost, 2003a; Stixrude and Bertelloni, 2011). However, additional processes such as dehydration melting above the 410-km discontinuity (Bercovici and Karato, 2003; Freitas et al., 2017) could locally redistribute and concentrate iron.

Tian et al. (2012) showed that at high pressures, adding 1.6 wt.% water and 6.7 mol% iron to wadsleyite simultaneously, decreases the compressional/shear wave speed by 4.48% and 6.11%, respectively. Considering this in light of the results of our study, we suggest that the joint effect of water in wadsleyite and iron-enriched olivine may explain the distance dependent polarity observations beneath the Northern Atlantic. It is worth noting that our few opposite polarities of $S^{410}S$ observations are consistent with the models that fit the $P^{410}P$ observations (Figure S7).

If instead of the distance-dependence polarity changes the regional distribution of polarities is considered, (the northern part of the study area shows mostly opposite polarities while the southern regions show mostly same polarity observations) we would find that Fe-enriched olivine overlying hydrous wadsleyite (Fig. 8k and l) could explain the northern half of our study area, compared with a less iron-enriched olivine-bearing layer in the southern part of the investigation area. However, it is not clear which dynamic or structural scenario could explain this difference in iron content between the northern and southern part. Since the number of observations are lower in the northern part than in the southern part, more high-resolution observations of 410 km underside reflections are needed. However, the current source-receiver combinations limit the number of observations and therefore currently preclude a distinction between the two scenarios of regional or compositional dependence of observed polarities. A combined study of transmitted waves from receiver function methods with reflected waves off the 410 km discontinuity may allow us to have a more comprehensive thermochemical interpretations of polarity behaviour at this boundary (Figure S8). More seismological observations from different regions would also be necessary but this goes beyond the goal of this paper and will require future investigations.

5. Conclusion

We used the polarities of precursor arrivals to PP/SS seismic waves that reflect off the 410 km discontinuity beneath the Northern Atlantic. A large number of source-receiver combinations have been used in order to collect a large dataset of reflection points beneath our investigation area. For each event with visible PP precursors the polarity of the PP phase is compared to the polarity of the precursor signal and we find several events where the polarity of the precursors are opposite to that of PP. There seems to be a dependency of the polarities on either the location of the reflection point (northern half compared with southern half of the investigation area) or on the distance between source and receiver. For the later dependency, the events with epicentral distances greater than 118 degrees mostly show opposite polarities, while for those with smaller epicentral distances the same polarity of the main phase and precursor signal is dominant.

Using the Zoeppritz equations, we analyzed more than 729 million combinations of density, compressional and shear wave velocities for both layers, above and below the 410 km discontinuity to find the best combination of velocities and densities that can explain the observations. The best-fitting models have a smaller contrast in density than AK135 or a pyrolite model, and a negative contrast in P-wave speed and S-wave speed across the discontinuity. The calculated reductions in both compressional and shear wave velocities go up to 13% but mostly fall within the range of 3–4% and 5–7% for P and S waves.

We test several scenarios to explain our observations using mineral physics experiments and thermodynamical modelling. Hydrous wadsleyite beneath anhydrous olivine can create reflection coefficients consistent with our observations, however, based on previous studies from mineral physics experiments, the amount of water is on the high side compared with estimates of the maximum water storage capacity of wadsleyite. We tested adding iron to either wadsleyite or olivine as a second possibility. We found that iron enrichment in olivine in combination with hydration of wadsleyite can lead to negative velocity contrasts across the phase transition and therefore cause polarity reversals. In this case, however, an additional process is needed to redistribute iron between both phases of olivine and wadsleyite. A combined effect of water and iron seems to be needed to explain our observations of distance-dependence polarities. While Fe-enriched north versus low-iron south could explain regional distribution of polarities, to make a clearer distinction between a regional effect versus a distance dependent effect of polarities of $P^{410}P$, more high-quality $P^{410}P$ and additionally $S^{410}S$ observations in the region would be needed.

Investigating other tectonic regions with dense coverage of PP and SS precursors such as Eurasia, Pacific or the Indian ocean in the future

will help to better understand the polarity behaviour of reflections off the mantle transition boundaries and possible sources of polarity reversals.

Acknowledgements

We would like to thank the editor Vernon Cormier and the anonymous reviewer for their insightful suggestions and comments which have improved the clarity and quality of the manuscript. Data were collected from the Incorporated Research Institute for Seismology (IRIS) and the Seismic Central Observatory (SZO) from Federal Institute for Geosciences and Natural Resources (BGR). Data analyses were performed with Seismic Handler (Stammler, 1993) and the Taup toolkit (Crotwell et al, 1999). Maps were generated using the Generic Mapping Tools (Wessel and Smith, 1995). MS was supported by DFG grant TH1530/10-1 and 10-2. LC was supported partly by DFG grant TH1530/5-1, NWO grant 016.VIDI.171.022 and ERC/FP grant 320639. JB was supported by DFG grant MA4534/3-1 and GRK2156/1. We would like to thank U. Hansen and S. Merkel for discussions on dynamics and mineralogy of the mantle.

Appendix A. Supplementary data

Supplementary data to this article can be found online at https://doi.org/10.1016/j.pepi.2018.11.007.

References

Akaogi, M., Ito, E., Navrotsky, A., 1989. Olivine-modified spinel-spinel transitions in the system Mg_2SiO_4-Fe_2SiO_4: calorimetric measurements, thermochemical calculation, and geophysical application. J. Geophys. Res.-Solid Earth 94 (B11), 15671–15685.

Andrews, J., Deuss, A., 2008. Detailed nature of the 660 km region of the mantle from global receiver function data. J. Geophys. Res. 113(B6). doi:10.1029/2007JB005111.

Bagley, B., Courtier, A., Revenaugh, J., 2009. Melting in the deep upper mantle oceanward of the Honshu slab. Phys. Earth Planet. Inter. 175, 137–144.

Benz, H.M., Vidale, J.E., 1993. Sharpness of upper-mantle discontinuities determined from high-frequency reflections. Nature 365, 147–150.

Bercovici, D., Karato, S., 2003. Whole-mantle convection and the transition-zone water filter. Nature 425, 39–44.

Bina, C.R., Helffrich, G.R., 1994. Phase transition Clapeyron slopes and transition zone seismic discontinuity topography. J. Geophys. Res. 99, 15853–15860.

Bolfan-Casanova, N., Keppler, H., Rubie, D.C., 2000. Water partitioning between nominally anhydrous minerals in the MgO-SiO_2-H_2O system up to 24GPa: implications for the distribution of water in the Earth's mantle. Earth Planet. Sci. Lett. 182, 209–221.

Bonatto, L., Schimmel, M., Gallart, J., Morales, J., 2013. Studying the 410-km and 660-km discontinuities beneath Spain and Morocco through detection of P-to-S conversions. Geophys. J. Int. 194, 920–935. https://doi.org/10.1093/gji/ggt129.

Bonatto, L., Schimmel, M., Gallart, J., Morales, J., 2015. The upper-mantle transition zone beneath the Ibero-Maghrebian region as seen by teleseismic Pds phases. Tectonophysics 663, 212–224.

Buchen, J., Marquardt, H., Speziale, S., Kawazoe, T., Boffa Ballaran, T., Kurnosov, A., 2018. High-pressure single-crystal elasticity of wadsleyite and the seismic signature of water in the shallow transition zone. Earth Planet. Sci. Lett. 498, 77–87.

Cammarano, F., Deuss, A., Goes, S., Giardini, D., 2005a. One-dimensional physical reference models for the upper mantle and transition zone: combining seismic and mineral physics constraints. J. Geophys. Res.-Solid Earth 110(B1). doi:10.1029/2004JB003272.

Cammarano, F., Goes, S., Deuss, A., Giardini, D., 2005b. Is a pyrolitic mantle compatible with seismic data? Earth Planet Sci. Lett. 232, 227–243.

Chambers, K., Woodhouse, J.H., Deuss, A., 2005. Topography of the 410-km discontinuity from PP and SS precursors. Earth Planet. Sci. Lett. 235, 610–622.

Chen, J., Inoue, T., Weidner, D.J., Wu, Y., Vaughan, M.T., 1998. Strength and water weakening of mantle minerals, olivine, wadsleyite and ringwoodite. Geophys. Res. Lett. 25, 575–578.

Chen, J., Inoue, T., Yurimoto, H., Weidner, D.J., 2002. Effect of water on olivine-wadsleyite phase boundary in the (Mg, $Fe)_2SiO_4$ system. Geophys. Res. Lett. 29. https://doi.org/10.1029/2001GL014429.

Cobden, L., Goes, S., Cammarano, F., Connolly, J.A.D., 2008. Thermochemical interpretation of one-dimensional seismic reference models for the upper mantle: evidence for bias due to heterogeneity. Geophys. J. Int. 175, 627–648.

Cobden, L., Goes, S., Ravenna, M., Styles, E., Cammarano, F., Gallagher, K., Connolly, J.A.D., 2009. Thermochemical interpretation of 1-D seismic data for the lower mantle: the significance of nonadiabatic thermal gradients and compositional heterogeneity. J. Geophys. Res. 114 (B11309).

Connolly, J.A.D., 1990. Multivariable phase-diagrams: an algorithm based on generalized thermodynamics. Am. J. Sci. 290, 666–718.

Connolly, J.A.D., 2005. Computation of phase equilibria by linear programming: a tool for geodynamic modeling and its application to subduction zone decarbonation. Earth Planet. Sci. Lett. 236, 524–541.

Courtier, A.M., Revenaugh, J., 2007. Deep upper-mantle melting beneath the Tasman and Coral Seas detected with multiple ScS reverberations. Earth Planet. Sci. Lett. 259 (1–2), 66–76.

Crotwell, H.P., Owens, T.J., Ritsema, J., 1999. The Taup Toolkit: flexible seismic travel-time and ray-path utilities. Seismol. Res. Lett. 70 (2), 154–160.

Day, E.A., Deuss, A., 2013. Reconciling PP and P'P' precursor observations of a complex 660 km seismic discontinuity. Geophys. J. Int. 194, 834–838.

Deschamps, F., Trampert, J., 2004. Towards a lower mantle reference temperature and composition. Earth Planet. Sci. Lett. 222, 161–175.

Deuss, A., Woodhouse, J.H., 2001. Seismic observations of splitting of the mid-transition zone discontinuity in Earth's mantle. Science 294, 354–357.

Deuss, A., Redfern, S.A.T., Chambers, K., Woodhouse, J.H., 2006. The nature of the 660-kilometer discontinuity in Earth's mantle from global seismic observations of PP precursors. Science 311, 198–201.

Deuss, A., 2007. Seismic observations of transition zone discontinuities beneath hotspot locations. Geol. Soc. Am. 430, 121–136.

Deuss, A., 2009. Global observations of mantle discontinuities using SS and PP precursors. Surv. Geophys. 30, 301–326.

Engdahl, E.R., van der Hilst, R., Buland, R.P., 1998. Global teleseismic earthquake relocation with improved travel times and procedures for depth determination. Bull. Seismol. Soc. Am. 88, 722–743.

Estabrook, C.H., Kind, R., 1996. The nature of the 660-kilometer upper-mantle seismic discontinuity from precursors to the PP phase. Science 274, 1179–1182.

Fei, H., Yamazaki, D., Sakurai, M., Miyajima, N., Ohfuji, H., Katsura, T., Yamamoto, T., 2017. A nearly water-saturated mantle transition zone inferred from mineral viscosity. Sci. Adv. 3, e1603024.

Fei, Y., Van Orman, J., Li, J., van Westrenen, W., Sanloup, C., Minarik, W., Hirose, K., Komabayashi, T., Walter, M., Funakoshi, K., 2004. Experimentally determined postspinel transformation boundary in Mg2SiO4 using MgO as an internal pressure standard and its geophysical implications. J. Geophys. Res.-Solid Earth, 109(B2). doi:10.1029/2003JB002562.

Flanagan, M.P., Shearer, P.M., 1998. Global mapping of topography on transition zone velocity discontinuities by stacking SS precursors. J. Geophys. Res.- Solid Earth 103, 2673–2692.

Flanagan, M.P., Shearer, P.M., 1999. A map of topography on the 410-km discontinuity from PP precursors. Geophys. Res. Lett. 26, 549–552.

Freitas, D., Manthilake, G., Schiavi, F., Chantel, J., Bolfan-Casanova, N., Bouhifd, M.A., Andrault, D., 2017. Experimental evidence supporting a global melt layer at the base of the Earth's upper mantle. Nat. Commun. 8 (1), 2168.

Frost, D.J., 2003a. Fe^{+2}-Mg partitioning between garnet, magnesiowüstite, and (Mg, $Fe)_2Si_O4$ phases of the transition zone. Am. Mineral. 88, 387–397.

Frost, D.J., 2003b. The structure and sharpness of (Mg, $Fe)_2SiO_4$ phase transformations in the transition zone. Earth Planet. Sci. Lett. 216, 313–328.

Frost, D.J., 2008. The upper mantle and transition zone. Elements 4, 171–176.

Frost, D.J., Dolejs, D., 2007. Experimental determination of the effect of H_2O on the 410-km seismic discontinuity. Earth Planet. Sci. Lett. 256, 182–195.

Gossler, J., Kind, R., 1996. Seismic evidence for very deep roots of continents. Earth Planet. Sci. Lett. 138, 1–13.

Gu, Y.J., An, Y., Sacchi, M., Schultz, R., Ritsema, J., 2009. Mantle reflectivity structure beneath oceanic hotspots. Geophys. J. Int. 178, 1456–1472.

Gu, Y.J., Dziewonski, A.M., Ekström, G., 2001. Preferential detection of the Lehmann discontinuity beneath continents. Geophys. Res. Lett. 28, 4655–4658.

Gu, Y.J., Dziewonski, A.M., 2002. Global variability of transition zone thickness. J. Geophys. Res.-Solid Earth 107 (B7) ESE2-1 – ESE2-17.

Gurrola, H., Minster, J.B., 2000. Evidence for local variations in the depth to the 410 km discontinuity beneath Albuquerque, New Mexico. J. Geophys. Res. 105, 10847–10856.

Helffrich, G.R., 2000. Topography of the transition zone seismic discontinuities. Rev. Geophys. 38, 141–158.

Helffrich, G.R., Wood, B.J., 1996. 410 km discontinuity sharpness and the form of the olivine α-β phase diagram: resolution of apparent seismic contradictions. Geophys. J. Int. 126 (2), F7–F12.

Hill, R., 1952. The elastic behaviour of a crystalline aggregate. Proc. Phys. Soc. London Sect. A. 65, 349–354.

Hirose, K., 2002. Phase transitions in pyrolitic mantle around 670-km depth: Implications for upwelling of plumes from the lower mantle. J. Geophys. Res.-Solid Earth 107(B4) ECV3-1 – ECV3-13. doi:10.1029/2001JB000597.

Hirschmann, M.M., 2006. Water, melting, and the deep Earth H_2O cycle. Annu. Rev. Earth Planet. Sci. 34, 629–653.

Houser, C., Masters, G., Flanagan, M., Shearer, P., 2008. Determination and analysis of long-wavelength transition zone structure using SS precursors. Geophys. J. Int. 174 (1), 178–194.

Huang, X., Xu, Y., Karato, S.I., 2005. Water content in the transition zone from electrical conductivity of wadsleyite and ringwoodite. Nature 434, 746–749.

Irifune, T., Nishiyama, N., Kuroda, K., Inoue, T., Isshiki, M., Utsumi, W., Funakoshi, K., Urakawa, S., Uchida, T., Katsura, T., Ohtaka, O., 1998. The postspinel phase boundary in Mg_2SiO_4 determined by in situ x-ray diffraction. Science 279, 1698–1700.

Ita, J., Stixrude, L., 1992. Petrology, elasticity, and composition of the mantle transition zone. J. Geophys. Res.-Solid Earth 97 (B5), 6849–6866.

Ito, E., Takahashi, E., 1989. Postspinel transformations in the system Mg_2SiO_4-Fe_2SiO_4 and some geophysical implications. J. Geophys. Res.-Solid Earth 94 (B8), 10637–10646.

Jackson, I., Rigden, S.M., 1998. Composition and temperature of the Earth's mantle:

seismological models interpreted through experimental studies of Earth materials. In: Jackson, I. (Ed.), The Earth's mantle, Composition, Structure and Evolution, pp 405–460. Cambridge Univ Press.
Jacobsen, S.D., Smyth, J.R., 2006. Effect of water on the sound velocities of ringwoodite in the transition zone. In: Jacobsen, S.D., van der Lee, S. (Eds.), Earth's deep water cycle. A, Geophys. Monogr., 168: 131-145, AGU, Washington DC, USA.
Jacobeit, E., Thomas, C., Vernon, F., 2013. Influence of station topography and Moho depth on the mislocation vectors for the Kyrgyz Broadband Seismic Network (KNET). Geophys. J. Int. 193, 949–959.
Jasbinsek, J.J., Dueker, K., 2007. Ubiquitous low-velocity layer atop the 410-km discontinuity in the northern Rocky mountains. Geochem. Geophys. Geosyst. 8. https://doi.org/10.1029/2007GC001661.
Jasbinsek, J.J., Dueker, K.G., Hansen, S.M., 2010. Characterizing the 410 km discontinuity low-velocity layer beneath the LA RISTRA array in the North America Southwest. Geochem. Geophys. Geosys. 11 (3), Q03008. https://doi.org/10.1029/2009GC002836.
Jenkins, J., Cottarr, S., White, R.S., Deuss, A., 2016. Depressed mantle discontinuities beneath Iceland: evidence of a garnet controlled 660 km discontinuity? Earth Planet Sci. Int. 433, 159–168.
Karato, S., 2006. Influence of hydrogen-related defects on the electrical conductivity and plastic deformation of mantle minerals: a critical review. In: Jacobsen, S.D., van der Lee, S. (Eds.), Earth's Deep Water Cycle, Geophys. Monogr. Ser., 168: 113-129, AGU, Washington DC, USA.
Katsura, T., Yamada, H., Nishikawa, O., Song, M., Kubo, A., Shinmei, T., Yokoshi, S., Aizawa, Y., Yoshino, T., Walter, M.J., Ito, E., Funakoshi, K., 2004. Olivine-wadsleyite transition in the system (Mg, $Fe_)2Si_O4$. J. Geophys. Res.-Solid Earth 109 (B2). https://doi.org/10.1029/2003JB002438.
Katsura, T., Ito, E., 1989. The system Mg_2SiO_4-Fe_2SiO_4 at high pressures and temperatures: precise determination of stabilities of olivine, modified spinel, and spinel. J. Geophys. Res.-Solid Earth 94(B11): 15663, 15670.
Kennett, B.L.N., Engdahl, E.R., 1991. Traveltimes for global earthquake location and phase identification. Geophys. J. Int. 105 (2), 429–465.
Kennett, B.L.N., Engdahl, E.R., Buland, R., 1995. Constraints on seismic velocities in the Earth from traveltimes. Geophys. J. Int. 122 (1), 108–124.
Kind, R., Yuan, X., Saul, J., Nelson, D., Sobolev, S.V., Mechie, J., Zhao, W., Kosarev, G., Ni, J., Achauer, U., Jiang, M., 2002. Seismic images of crust and upper mantle beneath Tibet: evidence for Eurasian plate subduction. Science 298, 1219–1221.
Kohlstedt, D.L., Keppler, H., Rubie, D.C., 1996. Solubility of water in the α, β and γ phases of $(Mg, Fe)_2SiO_4$. Contrib. Mineral. Petrol. 123, 345–357.
Krüger, F., Weber, M., 1992. The effect of low-velocity sediments on the mislocation vectors of the GRF array. Geophys. J. Int. 108 (1), 387–393.
Lawrence, J.F., Shearer, P.M., 2006. A global study of transition zone thickness using receiver functions. J. Geophys. Res.-Solid Earth 111 (B6). https://doi.org/10.1029/2005JB003973.
Lawrence, J.F., Shearer, P.M., 2008. Imaging mantle transition zone thickness with SdS-SS finite-frequency sensitivity kernels. Geophys. J. Int. 174 (1), 143–158.
Lessing, S., Thomas, C., Saki, M., Schmerr, N., Vanacore, E., 2015. On the difficulties of detecting PP precursors. Geophys. J. Int. 201, 1666–1681.
Li, B., Liebermann, R.C., 2000. Sound velocities of wadsleyite β-($Mg_{0.88}$, $F_{e0.1}2_)2Si_O4$ to 10 GPa. Am. Mineral. 85, 292–295.
Liu, Z., Park, J., Karato, S.I., 2016. Seismological detection of low-velocity anomalies surrounding the mantle transition zone in Japan subduction zone. Geophys. Res. Lett. 43, 2480–2487.
Maguire, P.K.H., et al., 2003. Geophysical project in Ethiopia studies continental breakup. EOS Trans. Am. Geophys. Un. 84, 342–343.
Mao, Z., Jacobsen, S.D., Frost, D.J., McCammon, C.A., Hauri, E.H., Duffy, T.S., 2011. Effect of hydration on the single-crystal elasticity of Fe-bearing wadsleyite to 12 GPa. Am. Mineral. 96, 1606–1612.
Mao, Z., Jacobsen, S.D., Jiang, F., Smyth, J.R., Holl, C.M., Frost, D.J., Duffy, T.S., 2008. Single-crystal elasticity of wadsleyite, β-Mg_2SiO_4, containing 0.37-1.66 wt% H_2O. Earth Planet. Sci. Lett. 268, 540–549.
Mao, Z., Jacobsen, S.D., Jiang, F., Smyth, J.R., Holl, C.M., Duffy, T.S., 2008b. Elasticity of hydrous wadsleyite to 12 GPa: Implications for Earth's transition zone. Geophys. Res. Lett. 35(L21305). doi:10.1029/2008GL035618.
Morais, I., Vinnik, L., Silveira, G., Kiselev, S., Matias, L., 2015. Mantle beneath the Gibraltar Arc from receiver functions. Geophys. J. Int. 200 (2), 1155–1171.
Niazi, M., Anderson, D.L., 1965. Upper mantle structure of western North America from apparent velocities of P waves. J. Geophys. Res. 70 (18), 4633–4640.
Pearson, D.G., Brenker, F.E., Nestola, F., McNeil, J., Nasdala, L., Hutchison, M.T., Matveev, S., Mather, K., Silversmit, G., Schmitz, S., Vekemans, B., Vincze, L., 2014. Hydrous mantle transition zone indicated by ringwoodite included within diamond. Nature 507, 221–224.
Petersen, N., Gossler, J., Kind, R., Stammler, L., Vinnik, L., 1993. Precursors to SS and structure of transition zone of the north-western Pacific. Geophys. Res. Lett. 20, 281–284.
Reiss, A.S., Thomas, C., van Driel, J., Heyn, B., 2017. A hot midmantle anomaly in the area of the Indian Ocean geoid low. Geophys. Res. Lett. 44 (13), 6702–6711.
Revenaugh, J., Sipkin, S.A., 1994. Seismic evidence for silicate melt atop the 410-km mantle discontinuity. Nature 369, 474–476.
Ringwood, A.E., Major, A., 1967. High-pressure reconnaissance investigations in the system Mg_2SiO_4- MgO -H_2O. Earth Planet. Sci. Lett. 2, 130–133.
Rost, S., Garnero, E.J., Williams, Q., 2008. Seismic array detection of subducted oceanic crust in the lower mantle. J. Geophys. Res.-Solid Earth 113(B6). doi:10.1029/2007JB005263.
Rost, S., Thomas, C., 2002. Array seismology: methods and applications. Rev. Geophys. 40 (3) 2–1 – 2–27. doi:10.1029/2000RG000100.
Rost, S., Thomas, C., 2009. Improving seismic resolution through array processing techniques. Surv. Geophys. 30, 271–299.
Rost, S., Weber, M., 2002. The upper mantle transition zone discontinuities in the Pacific as determined by short-period array data. Earth Planet. Sci. Lett. 204 (3–4), 347–361.
Rychert, C.A., Laske, G., Harmon, N., Shearer, P.M., 2013. Seismic imaging of melt in a displaced Hawaiian plume. Nat. Geosci. 6, 657–660.
Rychert, C.A., Schmerr, N., Harmon, N., 2012. The Pacific lithosphere-asthenosphere boundary: seismic imaging and anisotropic constraints from SS waveforms. Geochem: Geophys. Geosys. 13, (1). https://doi.org/10.1029/2012GC004194.
Saal, A.E., Hauri, E.H., Langmuir, C.H., Perfit, M.R., 2002. Vapour undersaturation in primitive mid-ocean-ridge basalt and the volatile content of Earth's upper mantle. Nature 419, 451–455.
Saki, M., Thomas, C., Merkel, S., Wookey, J., 2018. Detecting seismic anisotropy above the 410 km discontinuity using refelction coefficients of underside reflections. Physics Earth Planet. Int. 274, 170–183.
Saki, M., Thomas, C., Nippress, S., Lessing, S., 2015. Topography of upper mantle seismic discontinuities beneath the North Atlantic: The Azores, Canary and Cape Verde plumes. Earth Planet Sci. Lett. 409, 193–202.
Sawamoto, H., Weidner, D.J., Sasaki, S., Kumazawa, M., 1984. Single-crystal elastic properties of the modified spinel (Beta) phase of magnesium orthosilicate. Science 224, 749–751.
Schmandt, B., Dueker, K.G., Hansen, S.M., Jasbinsek, J.J., Zhang, Z., 2011. A sporadic low-velocity layer atop the western U.S. mantle transition zone and short-wavelength variations in transition zone discontinuities. Geichem. Geophys. Geosyst. 12, Q08014. https://doi.org/10.1029/2011GC003668.
Schmerr, N., Garnero, E., 2006. Investigation of upper mantle discontinuity structure beneath the central Pacific using SS precursors. J. Geophys. Res.-Solid Earth 111(B8). doi:10.1029/2005JB004197.
Schmerr, N., Garnero, E., 2007. Upper mantle discontinuity topography from thermal and chemical heterogeneity. Science 318, 623–626.
Schmerr, N., Thomas, C., 2011. Subducted lithosphere beneath the Kuriles from migration of PP precursors. Earth Planet. Sci. Lett. 311, 101–111.
Schweitzer, J., Fyen, J., Mykkeltveit, S., Kvaerna, T., 2002. Seismic arrays: in new manual of seismological observatory practice-NMSOP. IASPEI 481–532.
Shearer, P.M., 1991. Constraints on upper mantle discontinuities from observations of long-period reflected and converted phases. J. Geophys. Res.-Solid Earth 96 (B11), 18147–18182.
Shim, S.H., Duffy, T.S., Shen, G., 2001. The post-spinel transformation in Mg_2SiO_4 and its relation to the 660-km seismic discontinuity. Nature 411, 571–574.
Smyth, J.R., 1994Ss. A crystallographic model for hydrous wadsleyite (β-Mg_2SiO_4): an ocean in the Earth's interior? Am. Mineral. 79, 1021–1024.
Smyth, J.R., Frost, D.J., 2002. The effect of water on the 410-km discontinuity. Geophys. Res. Lett. 29 (10), 1. https://doi.org/10.1029/2001GL014418.
Speziale, S., Duffy, T.S., Angel, R.J., 2004. Single-crystal elasticity of fayalite to 12 GPa. J. Geophys. Res.-Solid Earth 109 (B12). https://doi.org/10.1029/2004JB003162.
Stammler, K., 1993. Seismic Handler: programmable multichannel data handler for interactive and automatic processing of seismological analysis. Comput. Geosci. 19, 135–140.
Stixrude, L., Bertelloni, C., 2005. Thermodynamics of mantle minerals – I. Physical properties. Geophys. J. Int. 162 (2), 610–632.
Stixrude, L., Bertelloni, C., 2011. Thermodynamics of mantle minerals – II. Phase equilibria. Geophys. J. Int. 184, 1180–1213.
Sun, S.S., 1982. Chemical-composition and origin of the Earth′s primitive mantle. Geochim. Cosmochim. Acta. 46, 179–192.
Tauzin, B., Debayle, E., Wittlinger, G., 2010. Seismic evidence for a global low-velocity layer within the Earth's upper mantle. Nat. Geosci. 3, 718–721.
Thio, V., Cobden, L., Trampert, J., 2016. Seismic signature of a hydrous mantle transition zone. Phys. Earth Planet. Inter. 250, 46–63.
Thomas, C., Billen, M.I., 2009. Mantle transition zone structure along a profile in the SW Pacific: thermal and compositional variations. Geophys. J. Int. 176 (1), 113–125.
Thomas, C., Wookey, J., Brodholt, J., Fieseler, T., 2011. Anisotropy as cause for polarity reversals of D″ reflections. Earth Planet. Sci. Lett. 307 (3–4), 369–376.
Thompson, D.A., Hammond, J.O.S., Kendall, J.M., Stuart, G.W., Helffrich, G.R., Keir, D., Ayele, A., Goitom, B., 2015. Hydrous upwelling across the mantle transition zone beneath the Afar triple junction. Geochem. Geophys. Geosyst. 16, 834–846.
Tian, L., Zhao, J., Liu, W., Liu, L., Liu, H., Du, J., 2012. Effect of iron on high pressure elasticity of hydrous wadsleyite and ringwoodite by first-principles simulation. High Pressure Res. 32 (3), 385–395.
Tschauner, O., Huang, S., Greenberg, E., Prakapenka, V.B., Ma, C., Rossman, G.R., Shen, A.H., Zhang, D., Newville, M., Lanzirotti, A., Tait, K., 2018. Ice-VII inclusions in diamonds: evidence for aqueous fluid in Earth's deep mantle. Science 359 (6380), 1136–1139.
van der Meijde, M., Marone, F., Giardini, D., van der Lee, S., 2003. Seismic evidence for water deep in Earth's upper mantle. Science 300, 1556–1558.
Vidale, J.E., Benz, H.M., 1992. Upper-mantle seismic discontinuities and the thermal structure of subduction zones. Nature 356, 678–683.
Vinnik, L., 1977. Detection of waves converted from P to SV in the mantle. Phys. Earth Planet. Int. 15 (1), 39–45.
Vinnik, L., Farra, V., 2002. Subduction low-velocity layer and flood basalts. Geophys. Res. Lett. 29(4) 8-1-8-4. doi:10.1029/2001GL014064.
Vinnik, L., Farra, V., 2007. Low S velocity atop the 410-km discontinuity and mantle plumes. Earth Planet. Sci. Lett. 262 (3–4), 398–412.
Vinnik, L., Kumar, M.R., Kind, R., Farra, V., 2003. Super-deep low-velocity layer beneath the Arabian plate. Geophys. Res. Lett. 30 (7), 1415–1418. https://doi.org/10.1029/2002GL016590.
Wang, J., Bass, J.D., Katsura, T., 2014. Elastic properties of iron-bearing wadsleyite to

17.7 GPa: implications for mantle mineral models. Phys. Earth Planet. Int. 228, 92–96.
Watt, J.P., Davies, G.F., O'Connell, R.J., 1976. The elastic properties of composite materials. Rev. Geophys. Space Phys. 14 (4), 541–563.
Wei, S.S., Shearer, P.M., 2017. A sporadic low-velocity layer atop the 410 km discontinuity beneath the Pacific Ocean. J. Geophys. Res Solid Earth 122, 5144–5159.
Weidner, D.J., 1985. A mineral physics test of a pyrolite mantle. Geophys. Res. Lett. 12 (7), 417–420.
Weidner, D.J., Wang, Y., 2000. Phase transformations: Implications for mantle structure. In: Karato, S., Forte, A.M., Liebermann, R.C., Masters, G., Stixrude, L. (Eds.), Earth's deep interior: mineral physics and tomography from the atomic to the global scale, Geophys. Monogr. Ser., 117: 215-235, AGU, Washington DC, USA.
Wessel, P., Smith, W.H.F., 1995. New version of Generic Mapping Tools released. Eos Trans. AGU 76, 329.
Williams, Q., Hemley, R.J., 2001. Hydrogen in the deep Earth. Annu. Rev. Earth Planet. Sci. 29, 365–418.
Wood, B.J., 1995. The effect of H_2O on the 410-Kilometer seismic discontinuity. Science 268, 74–76.
Wood, B.J., Rubie, D.C., 1996. The effect of alumina on phase transformations at the 660-kilometer discontinuity from Fe-Mg partitioning experiments. Science 273, 1522–1524.
Xu, Y., Poe, B.T., Shankland, T.J., Rubie, D.C., 1998. Electrical conductivity of olivine, wadsleyite and ringwoodite under upper-mantle conditions. Science 280, 1415–1418.
Xu, W., Lithgow-Bertelloni, C., Stixrude, L., Ritsema, J., 2008. The effect of bulk composition and temperature on mantle seismic structure. Earth Planet. Sci. Lett. 275 (1–2), 70–79.
Yu, Y., Gao, S.S., Liu, K.H., Yang, T., Xue, M., Le, K.P., 2017. Mantle transition zone discontinuities beneath the Indochina Peninsula: Implications for slab subduction and mantle upwelling. Geophys. Res. Lett. 44 (14), 7159–7167.
Zha, C.S., Duffy, T.S., Downs, R.T., Mao, H.K., Hemley, R.J., 1996. Sound velocity and elasticity of single-crystal forsterite to 16 GPa. J. Geophys. Res. 101, 17535–17545.
Zha, C.S., Duffy, T.S., Mao, H.K., Downs, R.T., Hemley, R.J., Weidner, D.J., 1997. Single-crystal elasticity of β-Mg_2SiO_4 to the pressure of the 410 km seismic discontinuity in the Earth's mantle. Earth Planet. Sci. Lett. 147, 9–15.
Zheng, Z., Romanowicz, B., 2012. Do double 'SS precursors' mean double discontinuities? Geophys. J Int. 191, 1361–1373.
Zoeppritz, K., 1919. On the reflection and penetration of seismic waves through unstable layers. Göttinger Nachr. 66–84.